参赛学生姓名: 李子玄

中学: 深圳中学

省份: 广东省

国家/地区: 中国

指导老师姓名: 胡剑, 付琛

指导老师单位: 深圳中学, 深圳大学

论文题目: Liquid Droplet Trajectories:

Harnessing Sound to Measure the Unseen

Liquid Droplet Trajectories: Harnessing Sound to Measure the Unseen

Zixuan Li

Shenzhen Middle School, Shenzhen, Guangdong Province, P. R. China

Abstract

Dry eye disease is a common chronic condition affecting the ocular surface, for which tear viscosity measurement plays a vital role in both diagnosis and management. However, the characteristically low viscosity and ultra-small volume of tear fluid (typically only 4–5 μ L) present considerable challenges for accurate viscosity assessment, which existing techniques are unable to address adequately.

In this study, a novel method was proposed and demonstrated for measuring the viscosity, this unseen property, of low-viscosity fluids by harnessing sound waves to control liquid droplet trajectories. Focused interdigital transducers were designed and fabricated to generate surface acoustic waves (SAWs), which induce an upward elongation of a sessile droplet positioned at the focal point. Through systematic experimental observation of droplet dynamics, optimal parameters for effective SAW generation were identified: a frequency of 18.41 MHz, a pulse length of 2 ms, a pulse interval of 2 s, and a peak-to-peak voltage of 165 mV. Under these conditions, jetting droplet velocities ranged from 0.35 m/s to 0.77 m/s, enabling the droplet to reach a glass plate positioned 3 mm above and form a stable liquid bridge.

A series of fluids was tested, including water and glycerol-water solutions at volume concentrations ranging from 2% to 40%. Following bridge formation, the filament neck thinned under the influence of surface tension until eventual breakup. This transient process was captured using a high-speed camera at 20000 fps, allowing precise measurement of the filament diameter. The half-time for the filament to reduce to half its initial diameter was observed to range between 1.20 ms and 2.25 ms. The Ohnesorge number, which quantifies the relative effects of viscosity, inertia, and surface tension, was determined to lie within the range of 0.0036 to 0.014. A correlation was subsequently established between the dimensionless half-time (normalized by the Rayleigh time) and the Ohnesorge number.

Finally, the technique was applied to characterize 2- μ L polyvinyl alcoholbased artificial tear samples. The measured viscosities averaged 1.65 \pm 0.88 mPa·s, demonstrating the potential of this approach for practical application in the future.

Keywords: viscosity measurement, surface acoustic waves, surface tension effect, liquid bridge, filament breakup

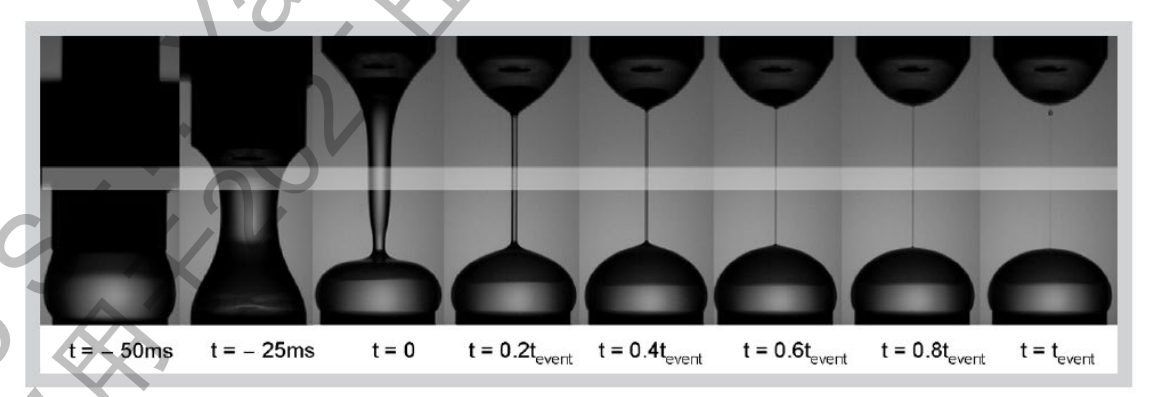
Contents

1.	Intro	oduction	1
2.	The	ory	3
	2.1	Principles of Surface Acoustic Waves (SAWs)	3
	2.2	Rheology of viscous fluid	4
	2.3	The basics of extensional flow techniques to measure fluid viscosity.	5
3.	Num	erical Simulation	7
	3.1	Numerical model	7
	3.2	SAWs simulation results	8
	3.3	The acoustic radiation pressure profile along the surface	9
	3.4	The effect of droplet size on the acoustic radiation pressure	11
4.	Expe	erimental Methods	11
	4.1	SAW device design and fabrication	11
	4.2	Experimental setup	13
	4.3	Hydrophobic coating of the SAW device	14
	4.4	The measurement method of filament radius	15
	4.5	Regression method of the parameters	15
5.	Expe	erimental Results	16
	5.1	Jetting performance of SAW devices at three frequencies	16
	5.2	The effects of driven signal amplitudes on liquid jetting behaviors	17
	5.3	The effect of the hydrophobic property of the opposing surface	19
	5.4	The effects of pulse length on liquid filament behaviors	19
	5.5	The break-up dynamics of liquid bridges driven by SAWs	21
	5.6	The curve of filament diameter versus time before breakup	28
	<i>5.7</i>	The relationship of normalized half-time with the Oh number	29
	5.8	The viscosities extracted from artificial tear liquid	30
6.	Disc	ussion	32
7.	Cond	clusion	35
Ac	know	ledgement	37
Re	feren	ces	39
An	nendi	x ^x $\Delta^{y}J$	41

1. Introduction

Dry eye disease (DED) is a common chronic ocular surface disease, affecting an estimated 5-50% of the global population [1]. DED patients suffer from ocular discomfort and visual disturbance, which severely impacts their quality of daily life. However, many people with DED remain unevaluated, undiagnosed, and untreated. DED is characterized by alterations in tear film composition and instability, resulting in abnormal tear viscosity. Measuring tear viscosity plays a crucial role in diagnosing and treating DED [2], as alterations in tear fluid rheology can indicate disease severity, differentiate subtypes, and guide personalized therapies, such as selecting high-viscosity artificial tears for enhanced symptom relief and ocular surface protection. However, current clinical methods for diagnosing DED, including slit-lamp examinations, staining tests, and tear breakup time assessments, are limited by poor precision, a lack of standardization, repeatability issues, invasiveness, and susceptibility to environmental factors, which often confound accurate diagnosis and optimal patient care.

The low viscosity and ultra-small sample volumes (often just 4-5 $\mu L)$ of tears pose significant challenges in measuring their viscosity. Traditional capillary viscometers and rotational viscometers require sample volumes far exceeding those typically available from tear collections. A recently developed filament extension technique employs two mechanical end-plates to extend a fluid sample into a filament. During this process, the filament radius decays to form a liquid bridge, which breaks up in a short time [2], as shown in Fig. 1.1. By observing the breakup dynamics, the sample's extensional viscosity could be extracted from the stress balance expression. However, the mechanical operation of these devices can induce vibrations that propagate throughout the filament, making repeatable readings impractical in low-viscosity fluids. These limitations, including high sample volume, invasiveness, and poor precision for biofluids, hinder tear rheology analysis in dry eye diagnostics.



In the filament extension technique, forming a stable fluid filament is critical for ensuring repeatability and accuracy of the measurements. Surface acoustic

wave (SAW) technology has emerged as a new method for manipulating droplets, including jetting, mixing, sorting, and atomization [3–5]. SAW propagates along the material surface, while the amplitude diminishes exponentially with depth into the substrate. It has been reported that the energy of SAWs is confined to a depth of three to four wavelengths into the substrate and can be concentrated to a spot using focusing transducers. Studies have shown that 20-MHz focused SAWs can generate an extraordinary fluid jetting phenomenon (Fig. 1.2) [6]. Since this type of energy from SAWs can drive significant jetting, the formation of a stable filament can be expected when two end plates hold the liquid or droplet, which forms the basic assumption of the present study.

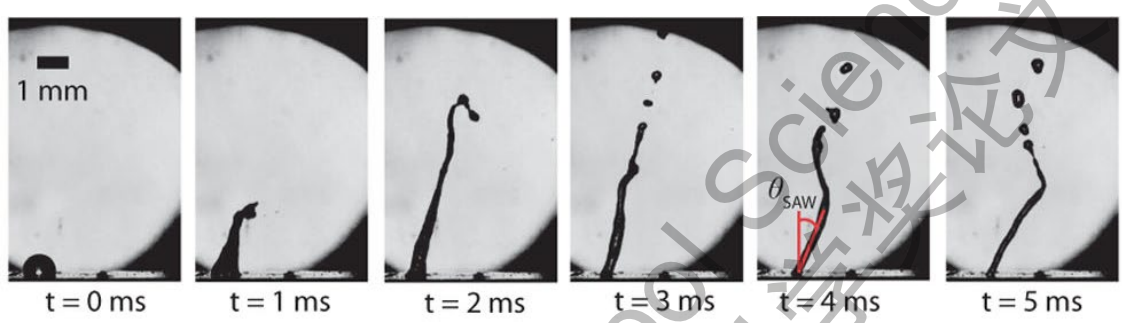


Figure 1.2. Fluid jetting of a water droplet generated by SAWs with a frequency of 20 MHz. The process is rapid, occurring at a microsecond scale. Source: [6].

In this study, I propose using SAWs to induce filament formation, which can be used to analyze the rheological properties of low-viscosity fluids in ultra-small volumes. As illustrated in Fig. 1.3, a sessile droplet is placed above the surface of a piezoelectric substrate and at the center of the paired interdigital transducers (IDT), which generate focused SAWs. The droplet is elongated upward, driven by the leaky SAWs. A glass plate is placed on the opposing side. Once the droplet reaches the opposing glass plate and forms a liquid bridge, the surface tension force contracts the filament, leading to uniaxial extensional flow until it breaks up. The viscosity of a liquid determines its resistance to flow, which directly influences how long a liquid filament can maintain its structure before breaking up. Therefore, the dynamics of filament breakup are directly related to the fluid viscosity, which can thus be calculated from the relationship between the filament diameter variation and time.

This study contained the following parts: 1) numerical simulation; 2) design and fabrication of SAW devices; 3) a parametric optimization of the excitation to form desired liquid bridges; 4) an investigation into the relationship between the filament diameter variation and the viscous coefficient; and 5) measurement of the viscosity of artificial tears with micro-liter volumes.

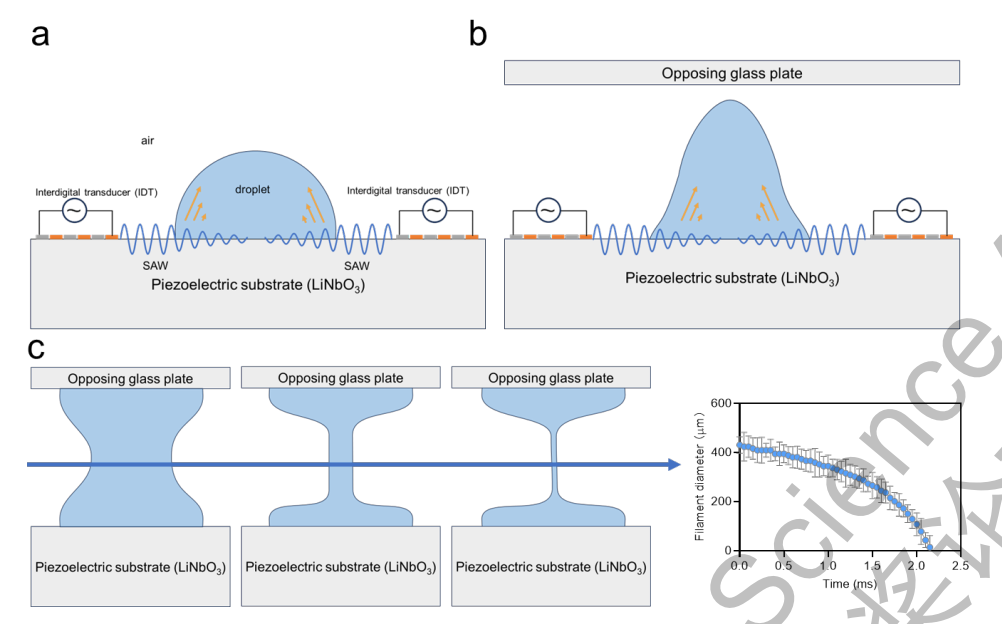


Figure 1.3. The illustration of the study design. (a) Surface acoustic waves (SAWs), generated by a pair of focused interdigital transducers (IDTs), leak into a sessile droplet. (b) The droplet is jetting and elongated upward, driven by the leaky SAWs. A glass plate is placed on the opposing side. (c) Once the droplet reaches the opposing glass plate and forms a liquid bridge, the surface tension force contracts the filament, leading to uniaxial extensional flow until it breaks up. The dynamics of filament breakup are directly related to the fluid viscosity, which can thus be derived from the relationship between the filament diameter variation and time.

2. Theory

2.1 Principles of Surface Acoustic Waves (SAWs)

Unlike vibrations that travel through the inside of a solid material, SAWs only move along the surface (Fig. 2.1). A typical example is the ripples that spread out when something hits the lake or the rolling waves moving across the earth's surface during an earthquake. The usual surface wave is called a Rayleigh wave. The amplitude of these waves exhibits exponential attenuation with increasing depth, resulting in the confinement of the majority of the acoustic energy within a shallow surface layer.

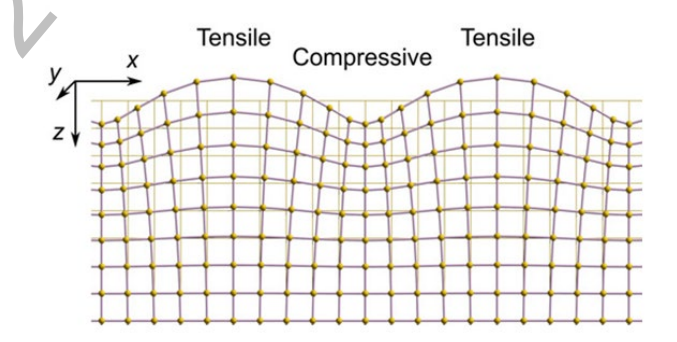


Figure 2.1. The schematic of Rayleigh waves shows the combination of tensile and compressive

waves. It should be noted that the waves are confined mainly to the surface. Source: [7]

As shown in Fig. 2.2, a sessile droplet is resting on a substrate in the path of SAWs. Diffraction occurs as SAW radiation encounters the edge of the droplet due to the difference between the speed of sound of the substrate c_{saw} and that of the fluid c_{fluid} . This causes a beam of acoustic energy to enter the droplet at an angle defined by the ratio of the two sound speeds called the Rayleigh angle θ_R .

$$\theta_R = \arcsin \frac{c_{fluid}}{c_{saw}}.$$
 (1)

This phenomenon is known as leaky SAW. With the speed of sound in the SAW device substrate being 3980 m/s and 1495 m/s for water, the necessary Rayleigh angle $\theta_R \approx 23^\circ$. Thus, the contact angle of the droplet must be larger than 23° to allow SAWs to leak into the droplet.

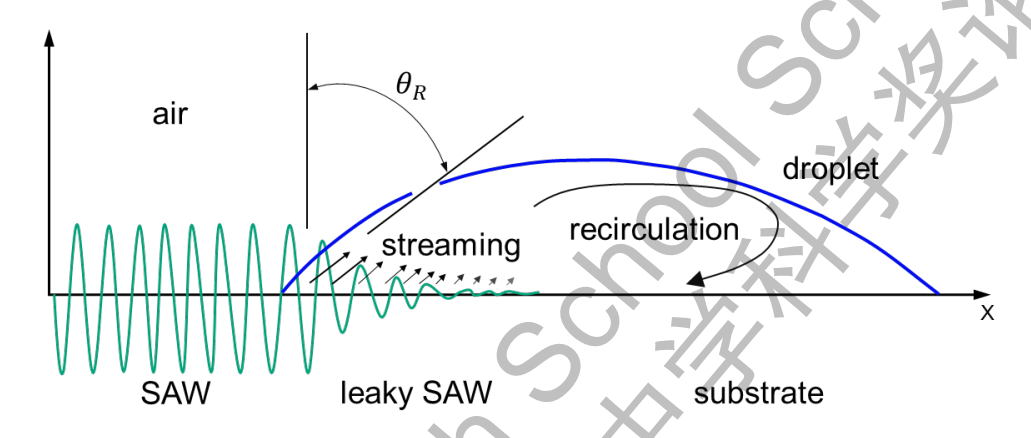


Figure 2.2. The schematic of SAWs leaking into a sessile droplet via the θ_R due to the difference between the speed of sound of the substrate and that of the fluid. The amplitude of the SAWs along the substrate surface attenuates exponentially as wave energy is transferred to the droplet.

2.2 Rheology of viscous fluid

All liquids comprise molecules. As these molecules move past each other during flow, internal friction develops, resulting in fluid resistance to flow, which is measured as viscosity. It is technically defined as the ratio of stress and imposed strain rate. In Newtonian fluids, this ratio remains constant; however, in non-Newtonian fluids, it varies across different strain rates.

There are two basic types of flow, shear flow and extensional flow. In shear flow, fluid components shear past one another (Fig. 2.3a), while in extensional flow, the fluid is stretched or elongated, causing its cross-sectional area to change (Fig. 2.3b). As illustrated in Fig. 2.3a, a shear force F acts on the fluid, yielding a shear stress (τ) , which is defined as the force (F) over a unit area (A). Therefore, the upper layer will move at a velocity u, while the bottom layer remains stationary, forming a shear strain γ . For a fluid, the constituent components can move relative to one another, generating a velocity gradient termed the shear rate or strain rate $\dot{\gamma}$:

$$\dot{\gamma} = \frac{du}{dx} \tag{2}$$

In Newton's law of viscosity, there is:

$$\tau = \eta \, \dot{\gamma},\tag{3}$$

where the proportional term η is the shear viscosity.

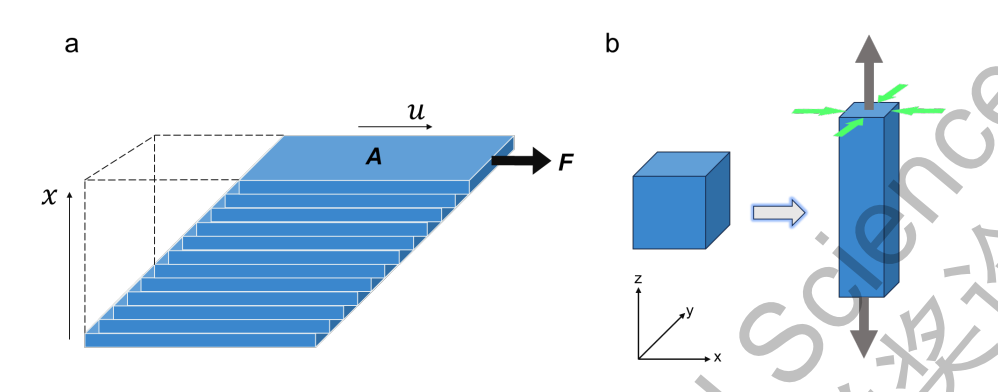


Figure 2.3. Illustration of shear flow and extensional flow.

Figure 2.3b shows the uniaxial extensional flow. The stretching of a finite volume in the z-axis (red arrows) to an elongated form is a uniaxial extensional flow. It can be seen that, through the conservation of volume, the dimensions in the xy-plane must contract (indicated by the green arrows). In the case of Newtonian fluid, there is a relationship of extensional viscosity $\bar{\eta}$ with shear viscosity η :

$$\bar{\eta} = 3\eta. \tag{4}$$

2.3 The basics of extensional flow techniques to measure fluid viscosity

The extensional flow techniques employ two mechanical end-plates to extend a fluid sample into a filament, allowing for the observation of its behavior as it thins to form a liquid bridge and potentially breaks. There are mainly two types of extensional flow techniques to measure fluid viscosity: the filament stretching extensional rheometer (FiSER) and the capillary breakup extensional rheometer (CaBER) [8,9]. In the FiSER method, an exponential velocity is imposed on the upper plate to create a uniaxial extensional flow with constant strain rate, in which transient extensional viscosity is calculated from the stress balance relationship of the tensile force exerted by the fluid column on the bottom stationary end plate and the filament radius at the axial midpoint of the filament. In the CaBER method, the rate of the end-plates opening is not controlled. Instead, the end-plates are rapidly moved apart to a fixed distance. While FiSER is recommended for characterizing viscous polymer solutions, CaBER is more suitable for lower viscosity solutions.

Figure 2.4 illustrates the basics of capillary break-up. First, I would like to introduce the concept of surface tension. In the Young–Laplace equation in spherical form, the pressure difference p across the interface between two static fluids, such as water and air, is formulated as,

$$p = -\frac{2\sigma}{R},\tag{5}$$

where σ is the surface tension and R is the curvature radius.

For a stable filament beyond a critical aspect ratio (defined by H/R0), the surface tension force P1 exerts a contractile stress on a fluid filament, which is resisted by P2. An extensional liquid with high aspect ratio H/R0 will lead to R1 < R2 and thus P1 > P2, causing instability and resulting in capillary breakup and filament collapse.

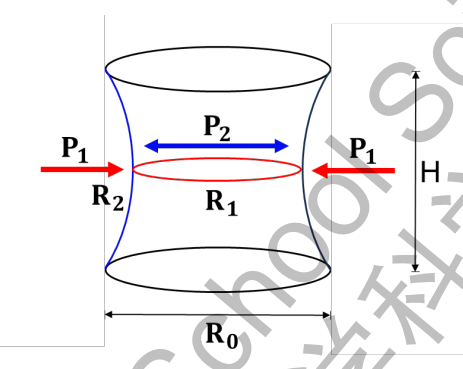


Figure 2.4. The diagram describes the basics that lead to capillary break-up, where R1 and P1 are the filament radius and radial pressure, respectively; R2 and P2 are the axial radius and pressure, respectively; and H and R0 are the height and distal radius of the filament, respectively.

For Newtonian extensional flows, the stress balance of the filament is governed by the equation, incorporating both inertia and viscous contributions [10]:

$$\frac{1}{2}\rho\dot{R}(t)^{2} = \frac{F(t)}{\pi R(t)^{2}} - \frac{\sigma}{R(t)} - 3\eta(\frac{-2\dot{R}(t)}{R(t)})$$
 (6)

The term on the left side of represents fluid inertia, and on the right-hand side F(t) represents the tensile force in the filament column. σ is the surface tension, and η is the viscosity of the fluid. I re-scaled the time by the Rayleigh time-scale τ_R and non-dimensionalized the radius with the initial R0, which are:

$$t^* = t/\tau_R, \ \tau_R = \sqrt{\frac{\rho R_0^3}{\sigma}}, R^* = R/R_0.$$
 (7)

Here I introduce the Ohnesorge number (Oh number), which assesses the effects of viscosity against inertia and surface tension,

$$Oh = \eta / \sqrt{\rho R_0 \sigma}. \tag{8}$$

Incorporating the Oh number, which characterizes the relative importance of a fluid's viscosity compared to its surface tension and inertia, Equation 6 is transformed into dimensionless filament radius and time as follows:

$$\left(\frac{dR^*}{dt^*}\right)^2 - \frac{120h}{R^*} \left(\frac{dR^*}{dt^*}\right) - \frac{2}{R^*} (2X - 1) = 0 \tag{9}$$

Since the rate of change in R^* is negative, taking the negative root only gives:

$$\frac{dR^*}{dt^*} = \frac{-60h}{R^*} \left[\left(1 + \frac{CR^*}{Oh^2} \right)^{\frac{1}{2}} - 1 \right], C = \frac{8}{144} (2X - 1)$$
 (10)

Separation of variables yields:

$$dt^* = \frac{-R^*}{60h} \left[\left(1 + \frac{CR^*}{0h^2} \right)^{\frac{1}{2}} - 1 \right]^{-1} dR^*$$
 (11)

By observing the filament radius dynamics during the break-up process, I could obtain another time parameter $t_{1/2}^*$, when the radius decays to half its initial radius. Integrating the above equation gives:

$$t_{1/2}^* = \int_1^{1/2} \frac{-R^*}{60h} \left[\left(1 + \frac{CR^*}{0h^2} \right)^{\frac{1}{2}} - 1 \right]^{-1} dR^*$$
 (12)

For water or low-viscosity fluids, the parameter X is 0.5197, as reported in previous studies [11]. The solution of Equation 12 is complex and can be approximated by the following equation [12]:

$$t_{1/2}^* = \frac{K_0 + K_1 O h + K_2 O h^2}{1 + O h}.$$
 (13)

 $t_{1/2}^*=\frac{K_0+K_1Oh+K_2Oh^2}{1+Oh}. \tag{13}$ where the parameters K_0,K_1 , and K_2 could be estimated through the regression of Equation 13. Then, based on the relationship of the normalized half-time $\,t_{1/2}^{*}$ with the Oh number, the extensional viscosity of unknown liquid could be obtained by:

$$\eta = 0h\sqrt{\rho R_0 \sigma}. (14)$$

3. Numerical Simulation

3.1 Numerical model

To investigate transmission of the acoustic field from SAW leaking into a liquid droplet, I conducted a numerical simulation to characterize the resulting acoustic radiation force acting upon the droplet. The simulation was performed using COMSOL Multiphysics 6.3 software, with the elastic wave module and frequency domain solver.

Leveraging the example in the COMSOL application gallery (Application ID: 139131) [13], a 2D model mimicking the situation of this study was used for simplicity, as shown in Fig. 3.1. The LiNbO₃ substrate is modeled by using the Piezoelectricity interface to couple electrostatics and solid mechanics. A lowreflecting boundary condition was employed to minimize wave reflections at the bottom, thereby simulating an open domain. In the solid domain, a linear elastic and isotropic model was applied; in the liquid domain, a thermo-viscous model was employed for the pressure acoustics. A sound soft boundary assigns a pressure of zero at the droplet-air boundary. SAWs are generated by applying an alternating voltage (10 Vpp) to the paired IDTs. The perfect-matching layers were used as absorbing boundary conditions to simulate infinite domains.

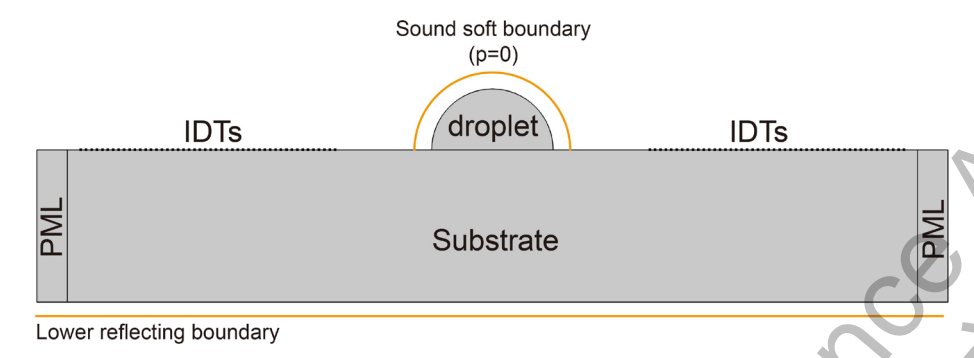


Figure 3.1. The 2D model used in the numerical simulation in COMSOL Multiphysics 6.3. A water droplet rests on the surface of the LiNbO $_3$ substrate. Paired IDTs are set on the surface.

The finite element mesh is generated using the default setting, allowing the physics interfaces to determine the meshing sequence. A Frequency Domain solver is employed to solve all the physical fields simultaneously. After obtaining the acoustic fields, including acoustic pressure p_1 and acoustic velocity v_1 in the droplet, the acoustic radiation pressure P_A acting on the droplet surface is calculated as follows:

$$P_A = \frac{1}{4}\kappa_0 p_1^2 - \frac{1}{4}\rho_0 v_1^2 \tag{15}$$

where κ_0 is the liquid compressibility, ρ_0 is the density. In the above equation, the first term is the acoustic potential energy density and the second term is the kinetic energy density.

3.2 SAWs simulation results

First, I simulated and compared the propagation of SAWs in the absence and presence of a water droplet. As shown in Fig. 3.2a, the paired IDTs could induce strong SAWs in the center. In contrast, when a droplet rests on the surface, the SAWs' intensity decreases, indicating energy leaking into the droplet (Fig. 3.2b). This study also numerically simulated the impact of three common air temperatures (10°C, 20°C, and 30°C) on the SAWs. The results, presented in Fig. 3.2(b-d), show that the acoustic attenuation decreases slightly as the temperature increases. This phenomenon occurs because, within this temperature range, the changes in the density and sound speed of water are minimal. Consequently, the acoustic impedance remains relatively constant, accounting for the observed trend.

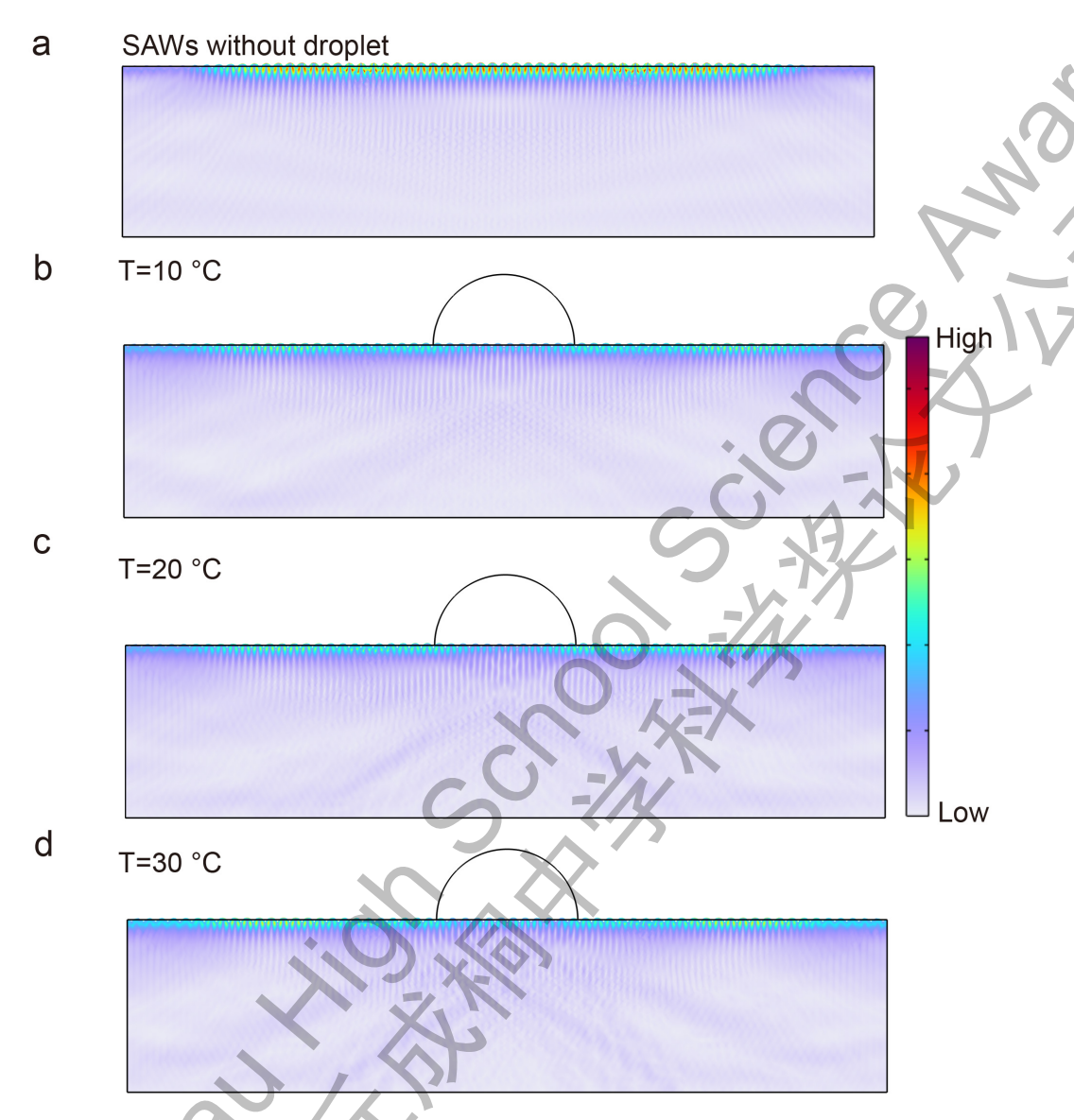


Figure 3.2. The SAWs simulated without (a) and with (b-d) a droplet at the temperatures of 10 $^{\circ}$ C, 20 $^{\circ}$ C and 30 $^{\circ}$ C. The frequency is 20 MHz.

3.3 The acoustic radiation pressure profile along the surface

Next, the acoustic field inside the droplet generated by the leakage of SAWs was compared for three frequencies: 10, 20, and 30 MHz. The radius of the water droplet is 1.0 mm. As shown in Fig. 3.3, regardless of the frequency, the SAWs generated by the paired IDTs propagate symmetrically into the droplet from both sides and converge at its apex, forming a region of high acoustic pressure.

When the SAW frequency is 10 MHz, the wavelength in water after leaking is approximately 150 μ m, as shown in Fig. 3.3a. There are about five to six wavelengths in the water droplet. As the frequency increases to 20 MHz or 30 MHz, an apparent Rayleigh angle of the leaking SAWs can be observed inside the droplet, as indicated by the acoustic pressure maps.

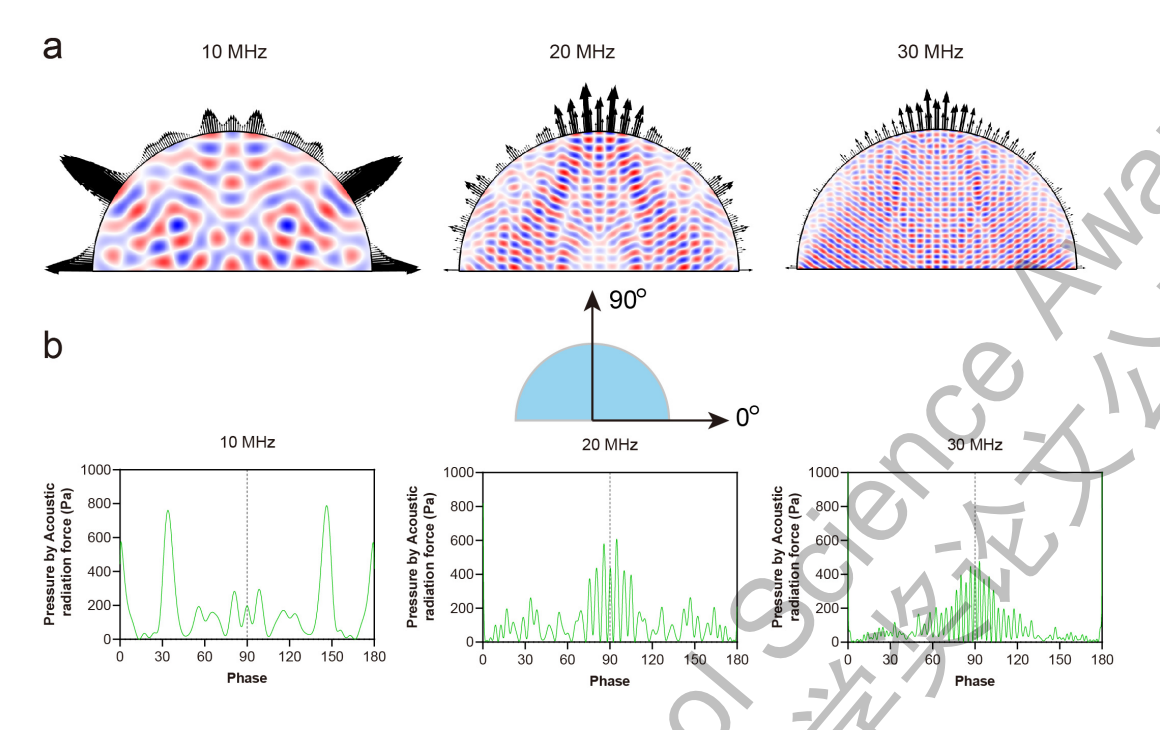


Figure 3.3. The acoustic pressure maps of SAWs leaking into the water droplet (a) and the acoustic radiation pressures along the droplet surface (b). Three frequencies are considered, and the radius R0 is 1.0 mm.

As shown in Fig. 3.3b, the black arrows, normal to the surface, represent the direction of the acoustic radiation pressure, while their length represents the magnitude of the force. As the frequency increases, the acoustic radiation pressure becomes increasingly concentrated at the droplet's apex. At frequency of 10 MHz, the acoustic radiation pressure at the apex is smaller than 200 Pa. At frequencies of 20 MHz and 30 MHz, the acoustic radiation pressure reached over 600 Pa and 400 Pa, respectively. For a droplet with a radius of 1.0 mm, the surface tension is calculated to be 145 Pa. Therefore, to form a droplet jet upward, the frequency of the SAWs should be set above 20 MHz.

3.4 The effect of droplet size on the acoustic radiation pressure

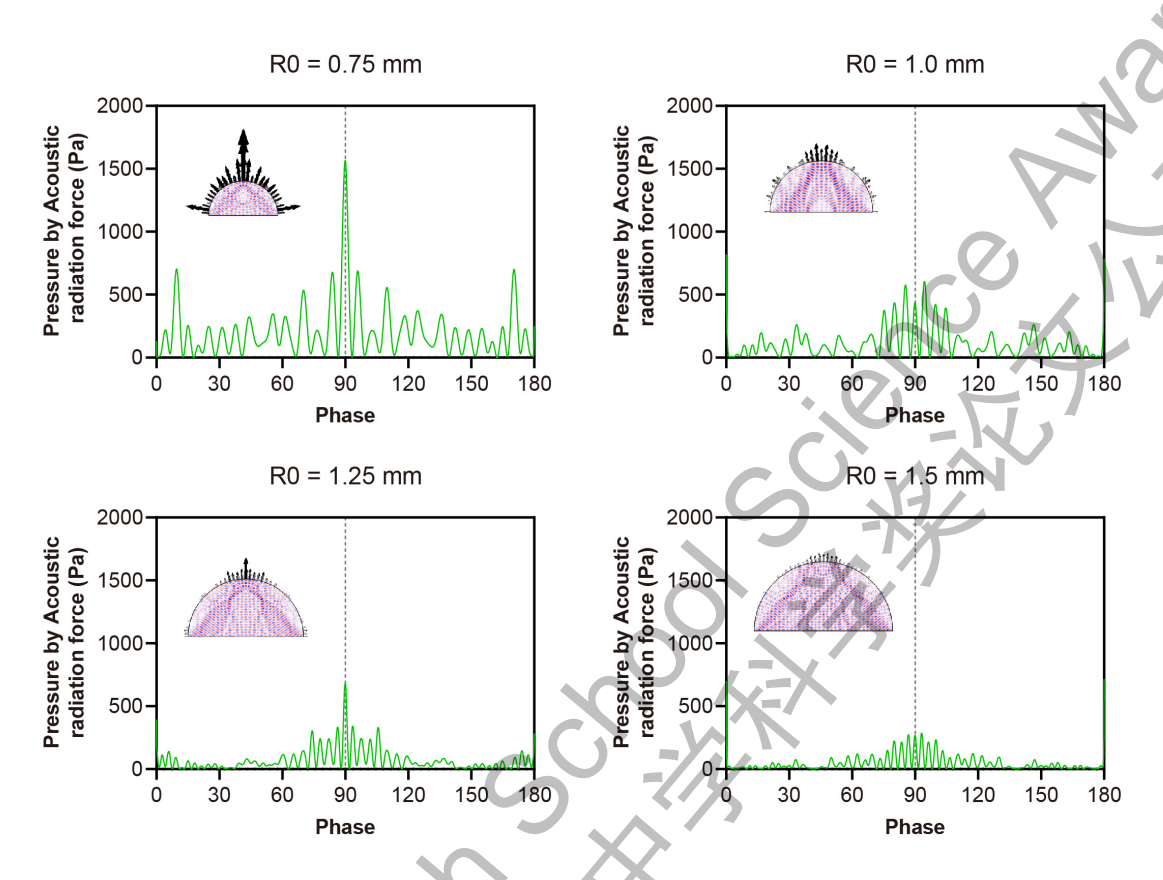


Figure 3.4. The acoustic radiation pressures along the surface of droplets with different radii: 0.75 mm, 1.0 mm, 1.25 mm, and 1.5 mm. The SAW frequency is 20 MHz.

The droplet's volume significantly influences the internal acoustic field distribution and the resulting acoustic radiation force following the leakage of the SAWs. As shown in Fig. 3.4, the simulation results indicate that for a droplet with a radius of 0.75 mm, a relatively sharp peak in acoustic radiation pressure can be formed at the droplet apex. However, when the droplet radius increases beyond 1.0 mm, the magnitude of the acoustic radiation pressure at the apex decreases by 50%. Although smaller droplet volumes facilitate jetting generation, droplets with a radius above 1.0 mm are more feasible based on practical operational considerations.

4. Experimental Methods

4.1 SAW device design and fabrication

In this study, SAWs were generated by a pair of focused interdigital transducers (IDTs) fabricated on a 0.5-mm-thick 128° y-x lithium niobate (LN) piezoelectric crystal, as described by previous studies [5,14]. Unlike straight IDTs, paired IDTs with circular arcs can concentrate acoustic energy at a specific point or within a

confined area. In our experiment, the SAW devices were designed with 25-pair or 30-pair aluminum IDT fingers of 100 nm thickness (Fig. 4.1). Two arcs were used: a 30° arc and a 90° arc. Three operating frequencies f_{saw} were investigated: 10 MHz, 20 MHz, and 30 MHz. The SAW frequency f_{saw} and the velocity in the substrate (3980 m/s) can decide the width and spacing between the IDT fingers, which are one fourth of the SAW wavelength λ as shown in Table 1.

Table 1	Designing param	eters of IDT	fingers
	~ 00.0 pa	00010 0112 1	

f_{saw}	λ	IDT width	Spacing	Pairs
10 MHz	398 µm	100 μm	100 μm	25
20 MHz	199 μm	50 μm	50 μm	30
30 MHz	132.67µm	35 μm	35 μm	30

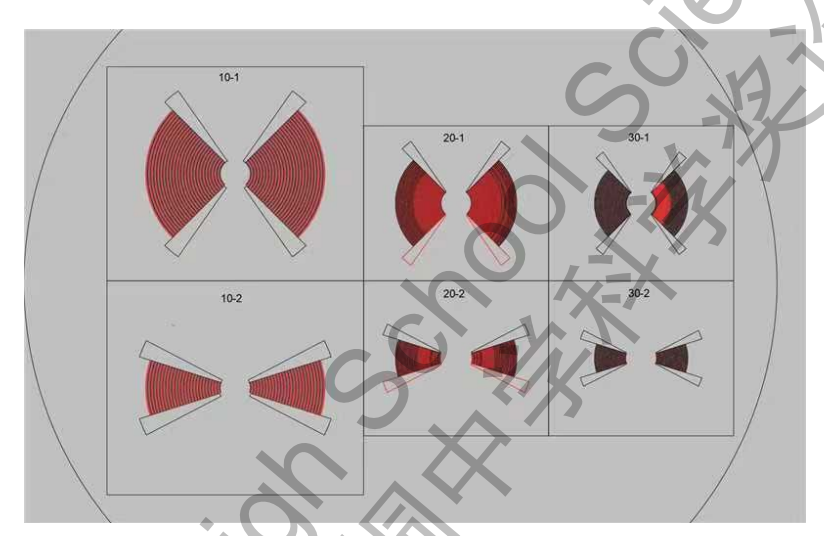


Figure 4.1. Different IDT designs with 35° arc and 90° arc at three frequencies (10 MHz: No. 10-1 and 10-2, 20 MHz: No. 20-1 and 20-2, and 30 MHz: No. 30-1 and 30-2).

Due to a lack of fabrication equipment, the SAW devices were fabricated by Dingxu Microcontrol Technology Corporation (Suzhou, China). After connecting the IDT electrodes to the self-made PCB circuit using conductive silver adhesive, the photographs of the SAW devices are shown in Fig. 4.2. The operating frequencies of the six SAW devices were determined using a network analyzer (Table 2).

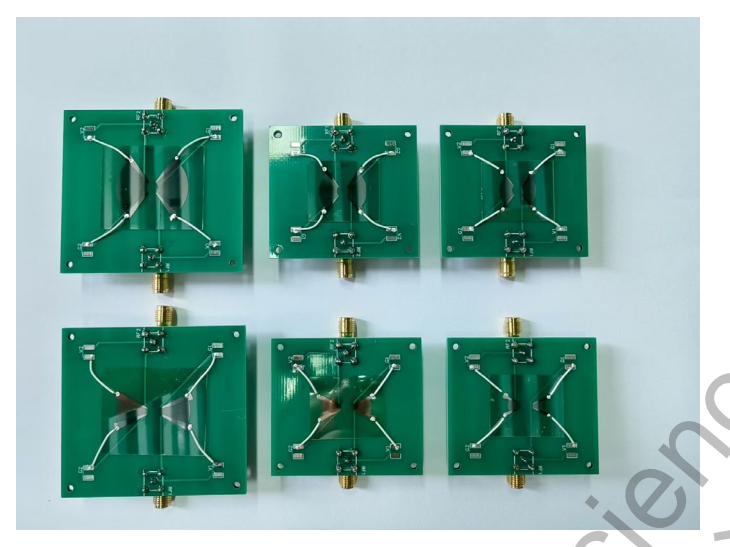


Figure 4.2. Photographs of the structure of the SAW devices for droplet driving. The upper row from left to right: No. 10-1, 20-1, and 30-1; The lower row from left to right: No. 10-2, 20-2, and 30-2.

Table 2. Operating frequencies of the six SAW devices

10-1	10-2	20-1	20-2 30-1	30-2
10.15 MHz	10.15 MHz	18.41 MHz	18.41 MHz 29.31 MHz	28.95 MHz

4.2 Experimental setup

The experimental setup is shown in Fig. 4.3. The driven signal was generated by a signal generator (AFG3102, Tektronix Inc., U.S.A.) and amplified by a 55-dB power amplifier (A150, ENI, U.S.A.). To visualize the liquid filament induced by SAW, a high-speed camera (Revealer S1315M, Agile Device Co., Ltd., China) equipped with 80W LED illumination and zoom lens (FF 100 mm, F2.8, CA-Dreamer Macro 2, Anhui Changgeng Optics Technology Co., Ltd, China) was used. The breakup process was observed and recorded at 20,000 frames per second. The resolution of the images captured was 768 pixels \times 664 pixels. Once the liquid bridge formed, it thinned under the effect of surface tension, and the subsequent temporal evolution of the filament radius was analyzed.

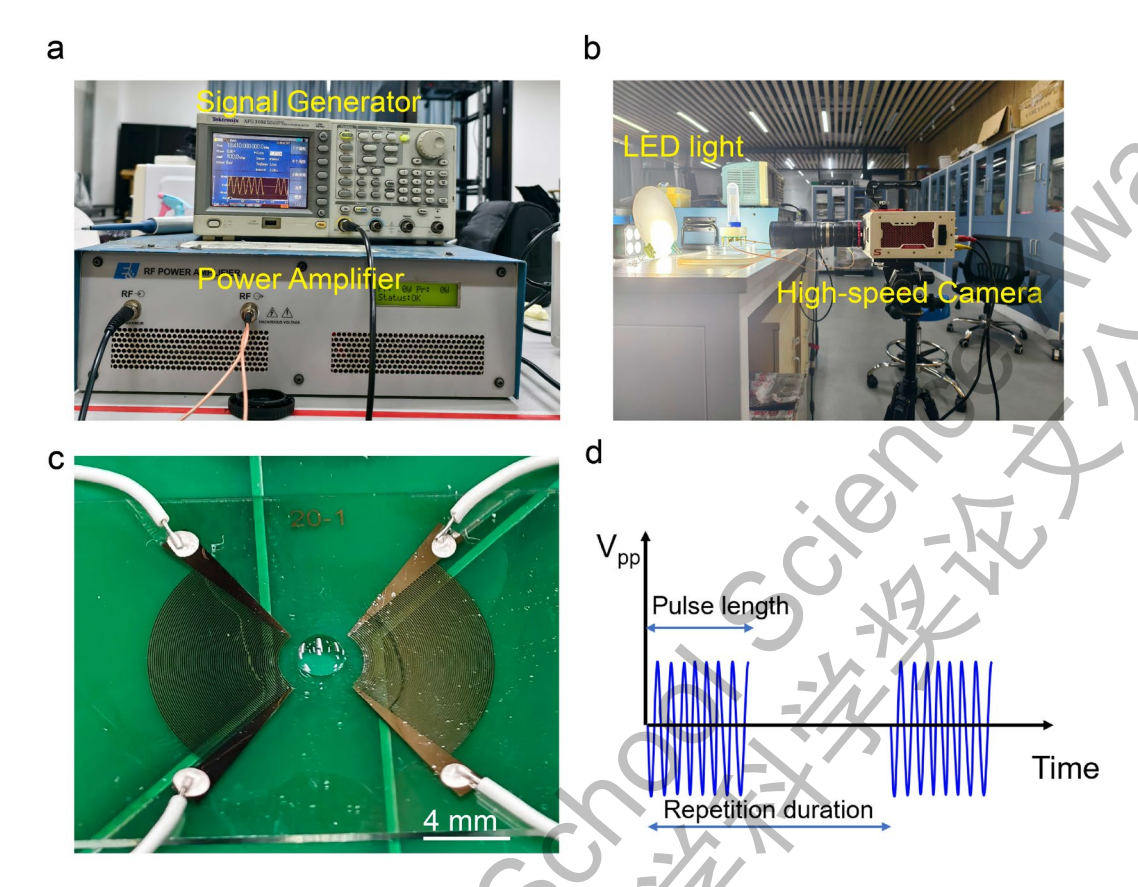


Figure 4.3. The experimental setup. (a) The driven signal was generated by a signal generator and amplified by a power amplifier. (b) The liquid bridge break-up process was recorded by a high-speed camera with a zoomed lens under LED illumination. (c). An enlarged view of a 2-µL droplet resting at the center of the paired IDT fingers. Scale bar: 4 mm. (d). An illustration of driven sinusoidal waves. "Burst" run mode was set, and the repetition duration was 2 s. Millisecond-scale cycles and micro-voltage peak-to-peak amplitudes (Vpp) of the driven sinusoidal signals were used to study the effects on liquid behaviors.

The water droplet with a volume of 3-4 μ L was manually placed at the center of the SAW device using a micropipette (Dragonlab, 0.1-10 μ L, China) as shown in Fig. 4.3c. Under the experimental setup of this study, the diameter of a 2.0-3.5 μ L water droplet ranges from 1.8 to 2.5 mm. Then, an opposing glass slide was placed on top of the device, with a 3 mm space between them, yielding a high aspect ratio of the liquid bridge larger than 1.20. To decrease the damage probability of the SAW device, a pulsed wave was used instead of a continuous wave. "Burst" run mode was set, and the repetition duration was 2 s (Fig. 4.3d). Millisecond-scale cycles and micro-voltage peak-to-peak amplitudes (Vpp) of the driven sinusoidal signal were used to study the effects on liquid behaviors.

4.3 Hydrophobic coating of the SAW device

The LN substrate is hydrophilic, causing liquid droplets to spread and resulting in a low contact angle. Therefore, a hydrophobic layer is needed to cover the device's focal point, allowing the droplet to rest with a sufficient contact angle. In this study,

the center of the paired IDT fingers was coated with a thin layer of Teflon material (0.3 μ L) by spinning at 1500 rpm and then drying at 65 °C overnight. Figure 4.4a shows the differences in the contact angles of water droplets resting on a glass without and with a hydrophobic coating. The contact angles of the five droplets in Fig. 4.4b were measured to be 103.1° \pm 2.3°, which were significantly larger than the Rayleigh angle θ_R (23°) and met the requirement of this study.

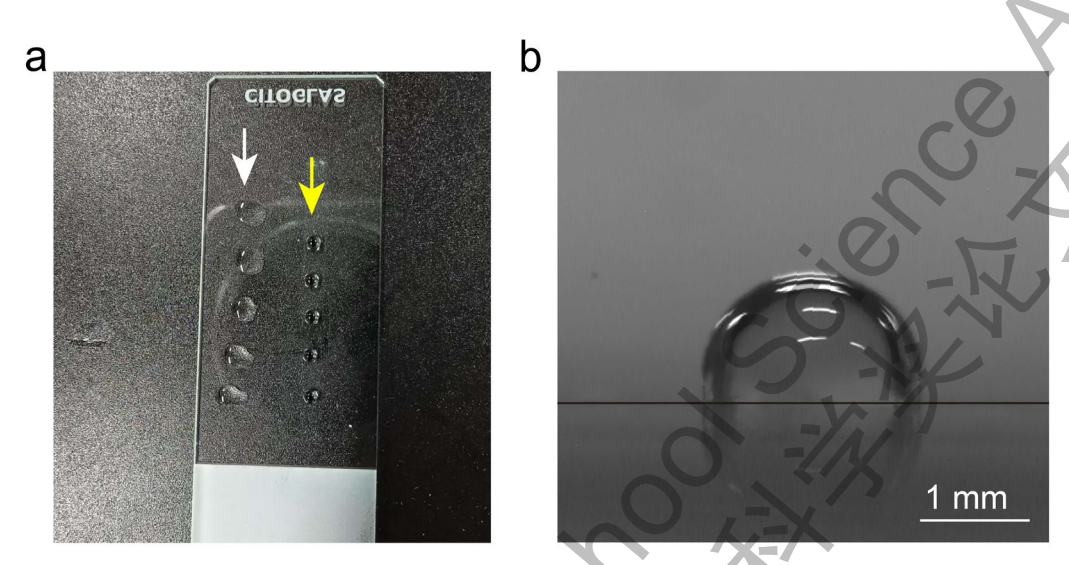


Figure 4.4. The resting water droplets on a glass after being hydrophobically coated with Teflon. (a) Top view of the droplets without (left, white arrow) and with (right, yellow arrow) hydrophobic coating layer. (b) Side view of a 3.0-µL droplet resting on top of the hydrophobic coating layer with a diameter of 2.04 mm. Scale bar: 1 mm.

4.4 The measurement method of filament radius

In this study, a single filament break-up event was captured by a high-speed camera at 20,000 frames per second (fps), providing a high temporal resolution of 0.05 ms per frame. Images were first converted to binary, black and white, and then the number of pixels corresponding to the narrowest region of the filament was measured using a custom MATLAB program (see Appendix). The filament diameter was subsequently calculated by applying the pixel-to-length ratio (6.538 μ m per pixel) derived from the calibration scale.

4.5 Regression method of the parameters

Following Equation 10, once the dimensionless half-time and the Ohnesorge number are obtained experimentally, the denominator is multiplied by the left-hand side of the equation. A quadratic polynomial is then fitted to the resulting data to yield estimates for the three unknown parameters using the software Graphpad Prism 9.0.

5. Experimental Results

5.1 Jetting performance of SAW devices at three frequencies

Pulsed sinusoidal waves with a 2-ms length were amplified by the power amplifier to drive the SAW device for generating SAWs. The six SAWs of different frequencies induced different behaviors of the droplets, as shown in Figure 5.1. With the same pulse length (2 ms) and amplitude (165 mVpp), the two 10-MHz SAW devices failed to induce noticeable droplet vibration, whereas the two 30-MHz devices resulted in only a slightly upward movement of the water droplet. In contrast, the droplet elongated by more than 4 mm after being stimulated by the No. 20-1 device. More strikingly, No. 20-2 generated the most intense jetting phenomenon, characterized by a rapidly rising liquid jet that culminated in the ejection of multiple secondary droplets.

Considering that adequate elongation of the water droplet, driven by the SAW device 20-1, is sufficient for this study, I proceeded with this device operating at 18.41 MHz for subsequent experiments.

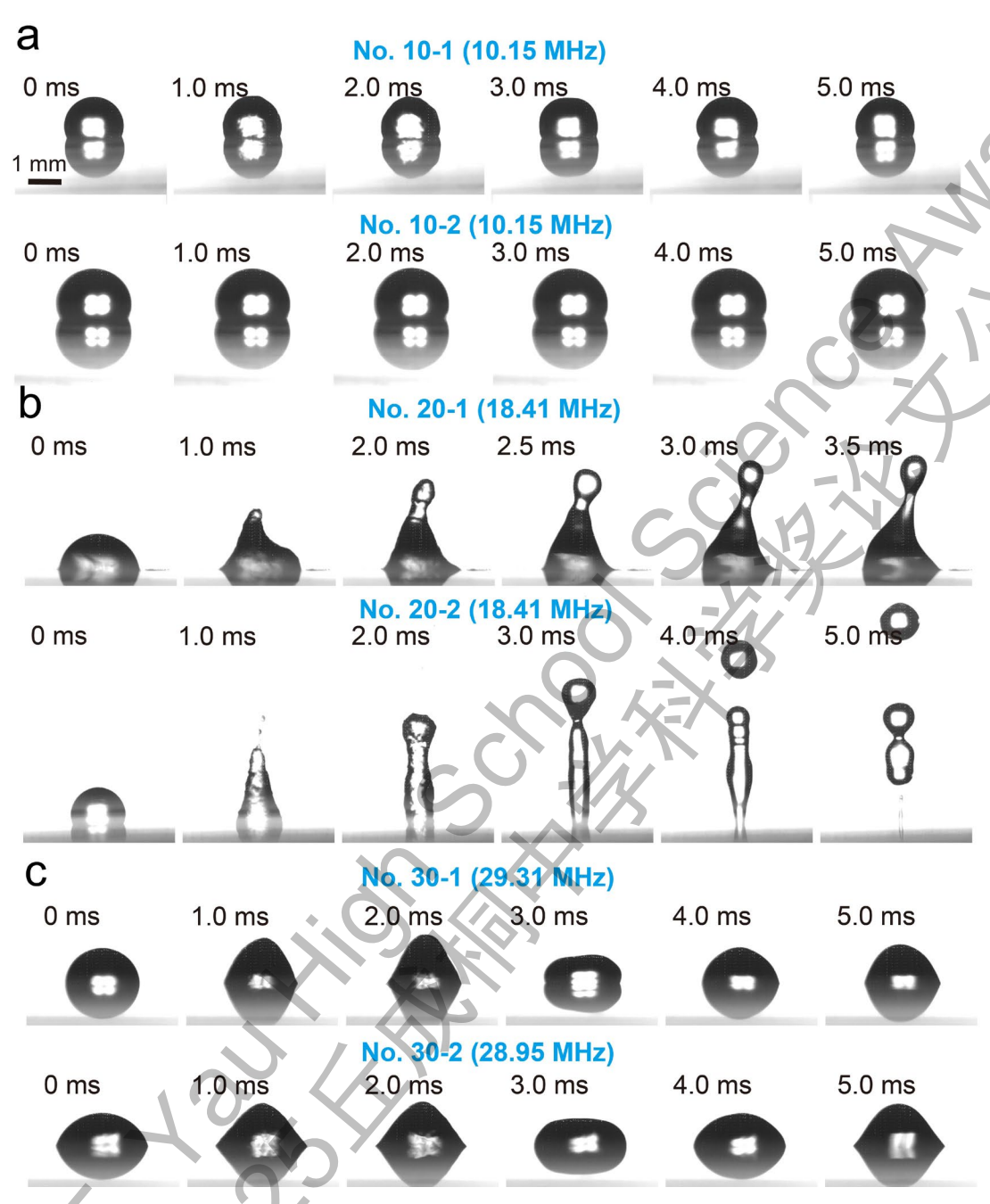


Figure 5.1. Montages of behaviors of water droplets subjected to a 2.0-ms SAW burst at the same amplitude (165 mVpp) but with different frequencies. (a) 10.15 MHz; (b) 18.41 MHz; (c) 29.31 and 28.95 MHz.

5.2 The effects of driven signal amplitudes on liquid jetting behaviors

To determine the optimal signal voltage for exciting the water droplet, I adjusted the peak-to-peak amplitude of the sinusoidal wave and observed the corresponding behavior of the droplet (Fig. 5.2). When a peak-to-peak voltage of 100 mV was applied, the droplet formed a small mound-like shape with a height of 1.5 mm by the end of the 2-ms burst. It then receded under the influence of gravity. At 125 mV, a similar mound formation was observed, though with a greater

height of 2.0 mm. Although the height was greater, an aspect ratio of 1.1 (for a 1.8 mm diameter droplet) was still insufficient to achieve the conditions necessary for liquid bridge formation. Therefore, I increased the voltage to 165 mV. As a result, with the 2-ms excitation, a sharp spike rapidly emerged at the top of the water droplet. After the burst ceased, the droplet continued to extend upward, exceeding 3 mm in height. Driven by inertia, the tip eventually pinched off, ejecting a small droplet.

This study involved mounting an opposing glass plate above the SAW device with a 3 mm spacing distance. This configuration required the droplet to achieve an aspect ratio of at least 1.67. Based on the above observations, a peak-to-peak voltage of 165 mV was found to be suitable, as it provided sufficient elongation to meet the requirement for stable liquid bridge formation. After the power amplification, the electrical power applied to the No. 20-1 SAW device was 7 W, as displayed on the power amplifier's screen.

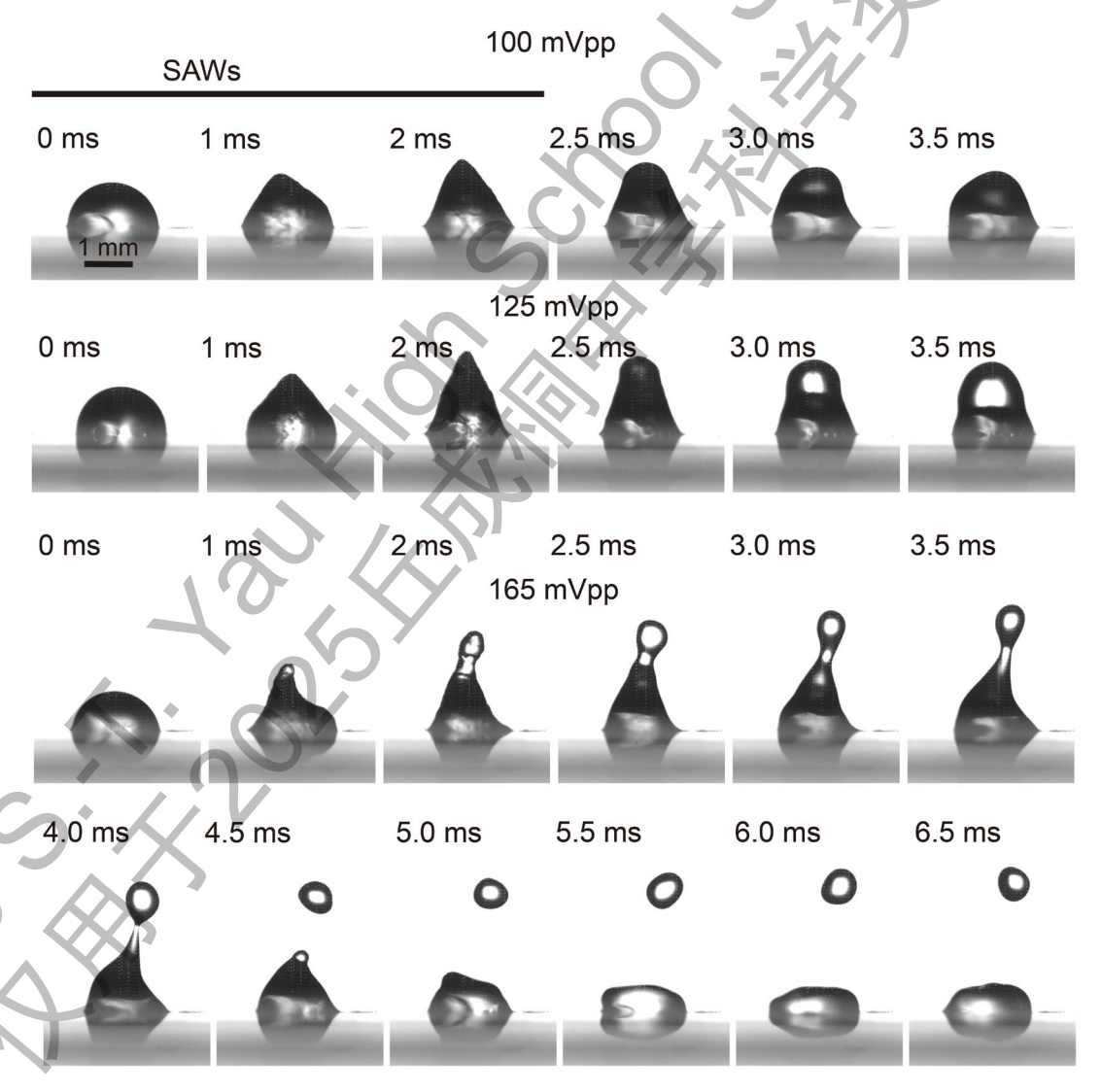


Figure 5.2. Montages of behaviors of water droplets subjected to a 2.0-ms SAW burst (18.41 MHz) at three different amplitudes: 100, 125, and 165 mVpp.

5.3 The effect of the hydrophobic property of the opposing surface

During the initial experiments, I used standard glass slides with hydrophilic surfaces. It was observed that when a water droplet was actuated by SAW excitation and came into contact with the opposing glass plate above, the droplet was entirely adsorbed onto the upper surface due to its hydrophilic nature, as shown in the montage in Fig. 5.3. As a result, a stable liquid filament could not be formed as desired. Therefore, the hydrophobic property of the opposing surface is critical to form a steady liquid bridge between the two surfaces. Initially, an attempt was made to coat the glass plate with Teflon material; however, the liquid filament would contract entirely and retract back into the parent drop by the surface tension force. This issue was ultimately resolved by applying a dust-free adhesive tape, which provided a suitable surface for stable bridge formation.

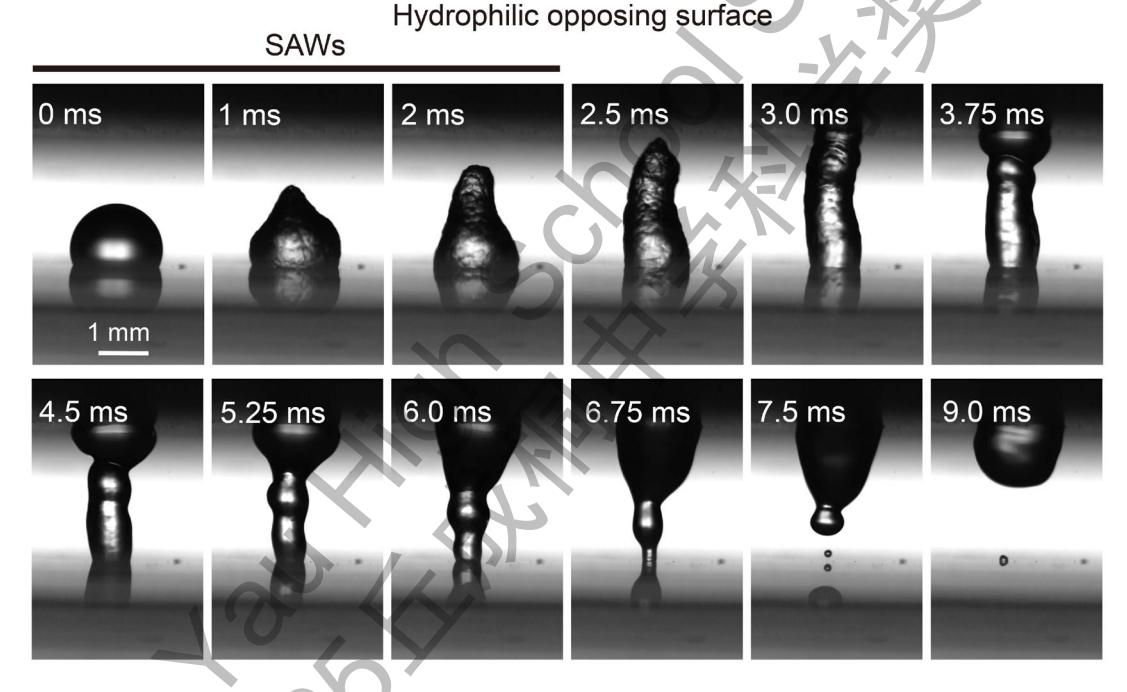


Figure 5.3. A montage of the behavior of a water droplet subjected to a 2.0-ms SAW burst when using a standard glass slide without hydrophobic coating. After the cessation of the SAW burst, a liquid bridge formed. However, the droplet was entirely adsorbed onto the upper surface due to its hydrophilic nature.

5.4 The effects of pulse length on liquid filament behaviors

In addition to the excitation voltage, the pulse length of the excitation sine wave is also a critical factor influencing the energy of the SAWs. A longer pulse length results in greater energy delivery. Therefore, to identify the optimal pulse length, a parametric study was conducted using three distinct pulse lengths: 1.5 ms, 2.0 ms, and 5.0 ms.

As shown in Fig. 5.4, at a 1.5-ms pulse length of the sinusoidal waves, a stub-

like deformation was created. In contrast, a 2.0-ms pulse length induced a significantly high peak of the droplet, resulting in the subsequent formation of a liquid bridge and filament. When excited with a pulse length of 5 ms, the water droplet rapidly elongated upward and made contact with the glass plate within 2 ms. However, since the pulse had not yet terminated, the droplet continued to be actuated upward by the acoustic radiation force. This resulted in most of the liquid being adsorbed onto the upper surface, leading to an uneven distribution.

Therefore, a pulse length of 2 ms was selected for subsequent experiments. This duration is sufficient to ensure the reliable formation of a stable liquid bridge, while also minimizing energy dissipation and potential damage to the SAW device, as well as extending the service life of the hydrophobic coating.

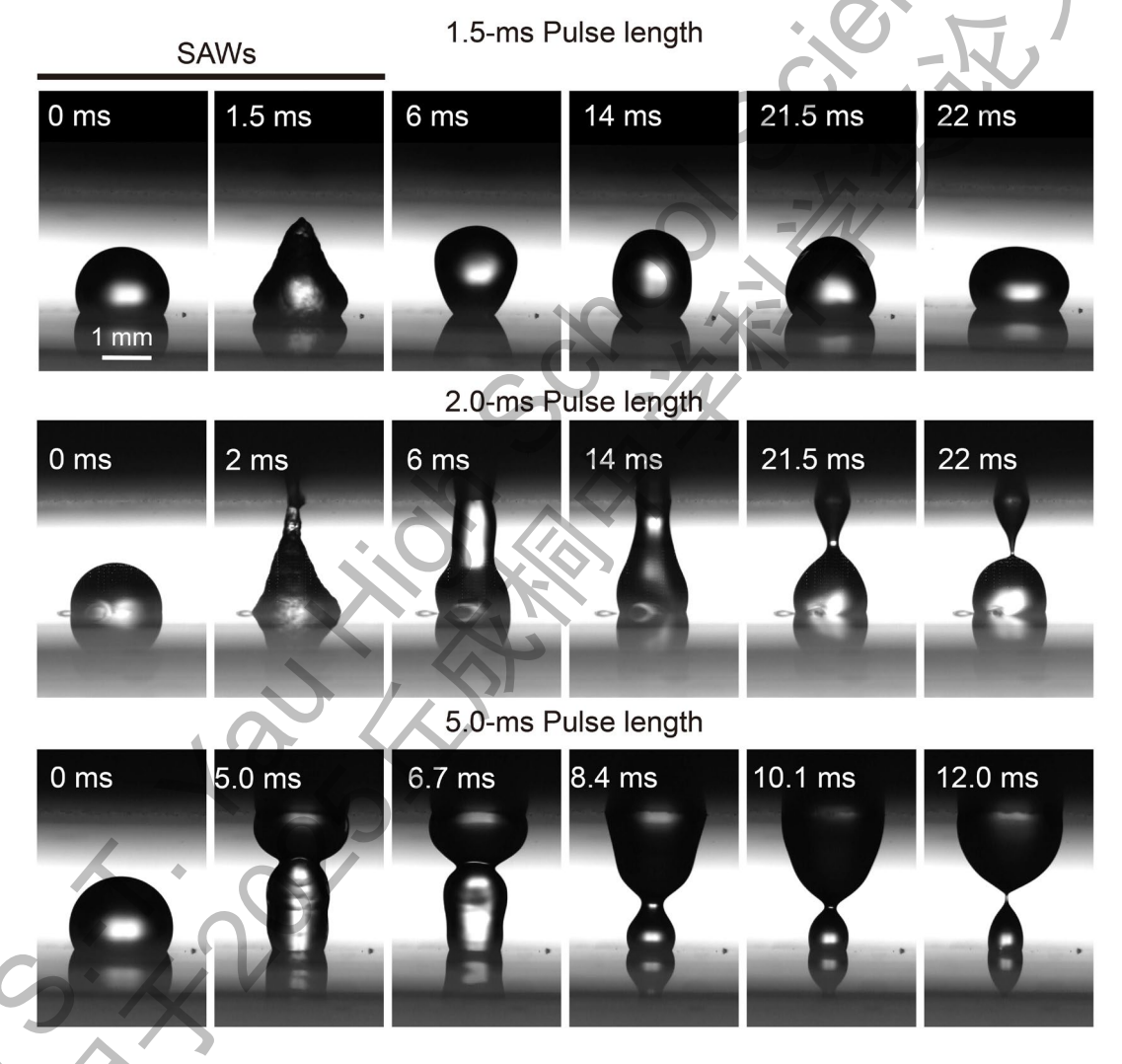


Figure 5.4. Montages of behaviors of water droplets subjected to 1.5-ms, 2.0-ms, and 5.0-ms SAW bursts. A stub-like deformation was created at a 1.5-ms pulse length. A liquid bridge and filament could be successfully generated by a 2.0-ms pulse length. An uneven distribution was induced by a 5.0-ms pulse length.

Based on these experimental observations of droplet behaviors, this study adopted the following parameters for generating SAWs in subsequent experiments:

a frequency of 18.41 MHz, a pulse length of 2 ms, a pulse interval of 2 s, and a peakto-peak voltage of 165 mV.

5.5 The break-up dynamics of liquid bridges driven by SAWs

Next, I conducted a series of experiments on the actuation of liquids with different viscosities using SAWs. The liquid samples included water, as well as glycerol-water mixtures at volume ratios of 2%, 10%, 16%, 18%, 20%, and 40%. Each liquid was tested in three replicates. The volume of the liquid droplet was 2.0 μL . For brevity's sake, the behavior of a single sample for each fluid type is presented in the following section.

1) Water

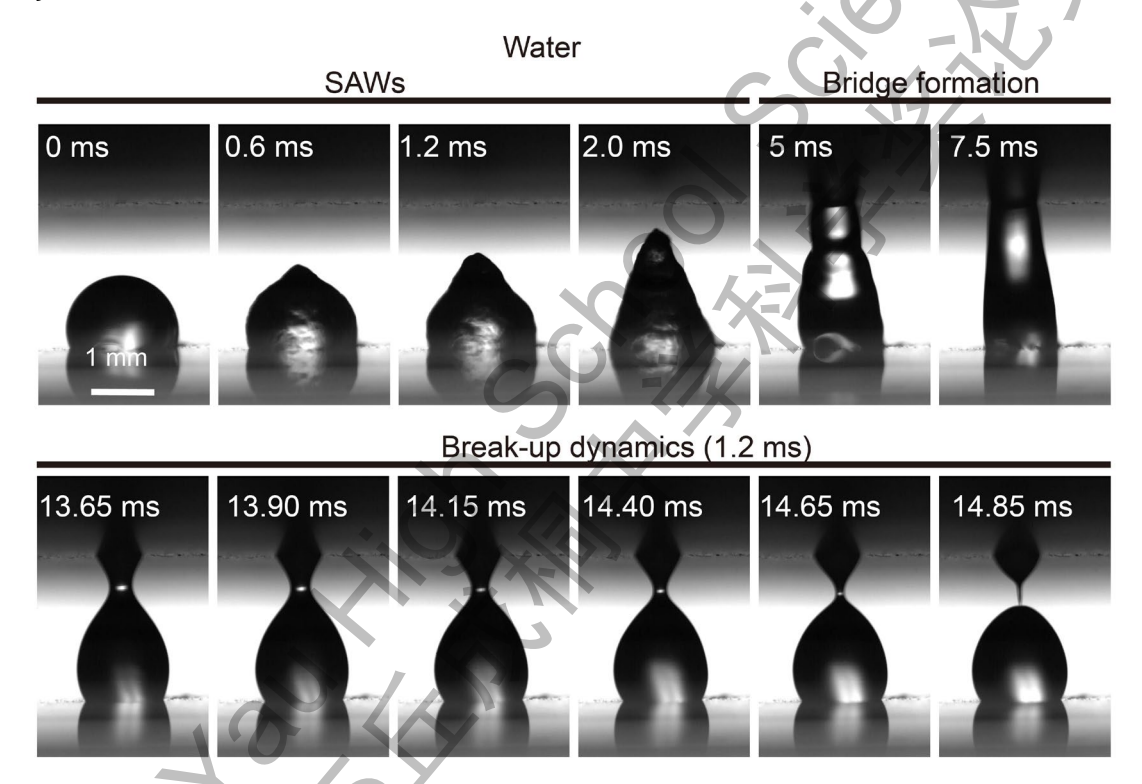


Figure 5.5. A montage of the behavior of a 2.0- μ L water droplet subjected to a 2.0- μ S SAW burst. After the cessation of the SAW burst and the formation of a liquid bridge, the surface tension force contracted the filament, driving uniaxial extensional flow until the filament broke apart. It took 1.2 ms for the liquid filament to break up from an initial diameter of 430 μ m.

As shown in the upper panel of Fig. 5.5, the water droplet was elongated until it reached the covering glass plate. Subsequently, a liquid bridge formed at the time point of 7.5 ms. Then, the liquid bridge contracted to create a filament because of the surface tension effect. It took 1.2 ms for the liquid filament to break up from an initial diameter of 430 μ m. The displacement and velocity of the droplet vertex were measured by tracing its position, as shown in Fig. 5.6. For this sample, during SAW excitation, the droplet continued to move upward. At ~3 ms, the vertex reached the opposing glass plate. The average velocity during the pulse length was

$0.3596 \pm 0.2025 \,\mathrm{m/s}.$

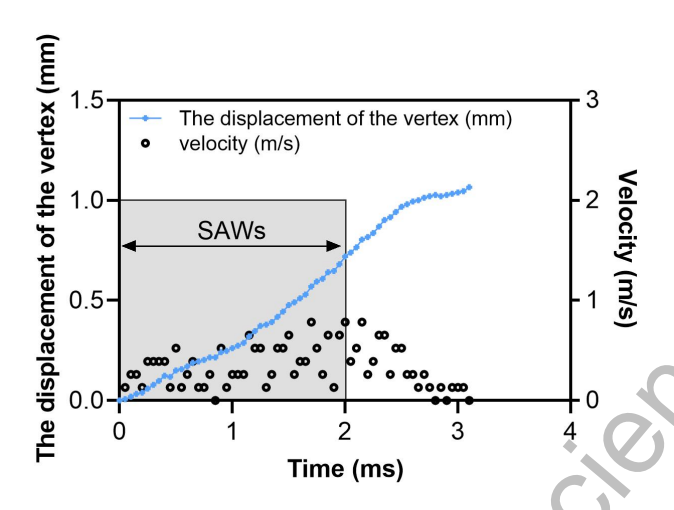


Figure 5.6. The displacement and velocity of the water droplet vertex.

2) 2% Glycerol-water solution

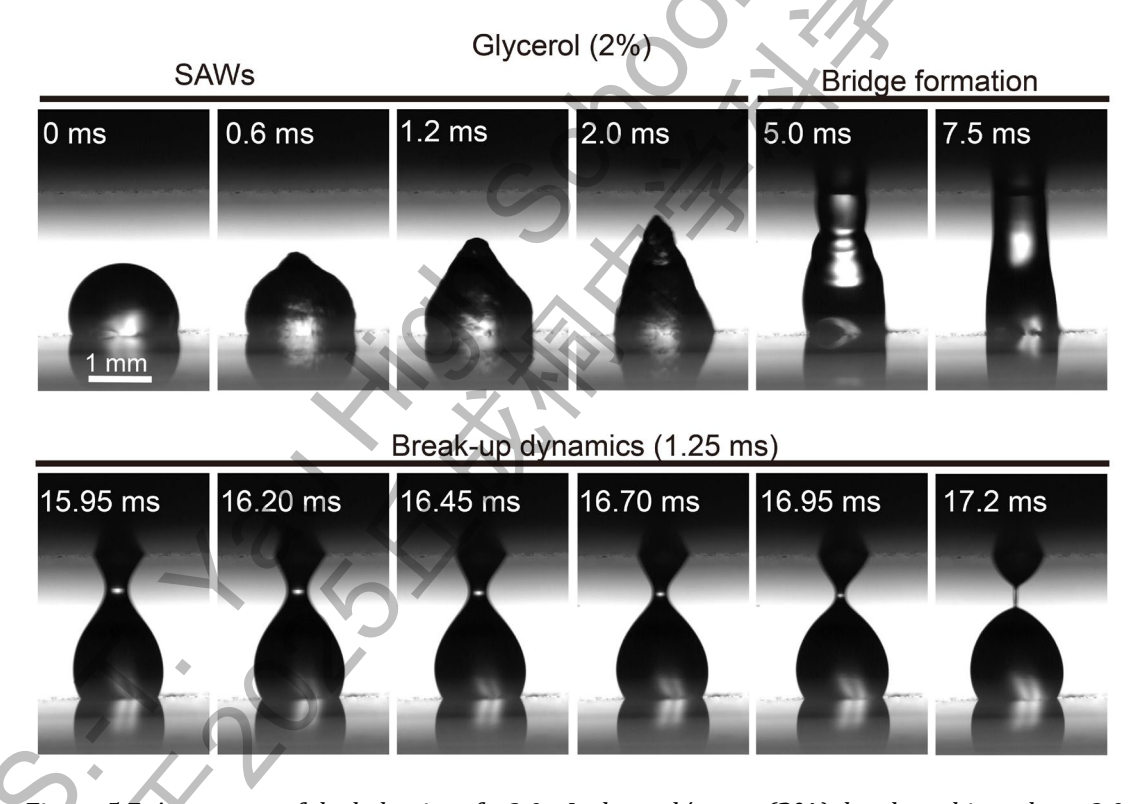


Figure 5.7. A montage of the behavior of a 2.0- μ L glycerol/water (2%) droplet subjected to a 2.0-ms SAW burst. It took 1.25 ms for the liquid filament to break up from an initial diameter of 430 μ m.

The dynamics of the 2% glycerol-water mixture were similar to those of pure water; as seen in Fig. 5.7, the difference is barely noticeable to the naked eye. However, quantitative analysis revealed that the filament breakup time for this mixture droplet was 1.25 ms, with a diameter of 430 μ m. Similar to the above water droplet, this 2% glycerol-water droplet continued to move upward within

2-ms SAW excitation. At \sim 3 ms, the vertex reached the opposing glass plate (Fig. 5.8). The average velocity during the pulse length was 0.3694 \pm 0.2006 m/s.

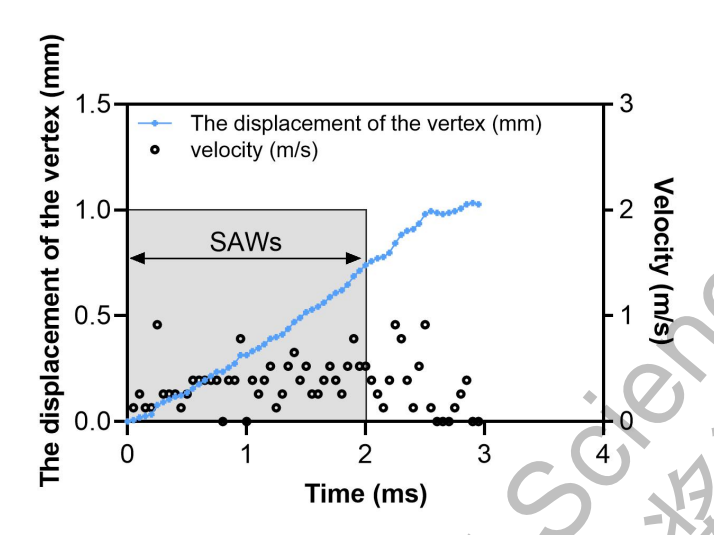


Figure 5.8. The displacement and velocity of the glycerol-water (2%) droplet vertex.

3) 10% Glycerol-water solution

When the glycerol volume fraction reached 10%, the filament breakup time of the liquid bridge driven by SAW was measured to be 1.55 ms from the diameter being 430 μ m (Fig. 5.9), which is significantly longer than that of the previous two samples.

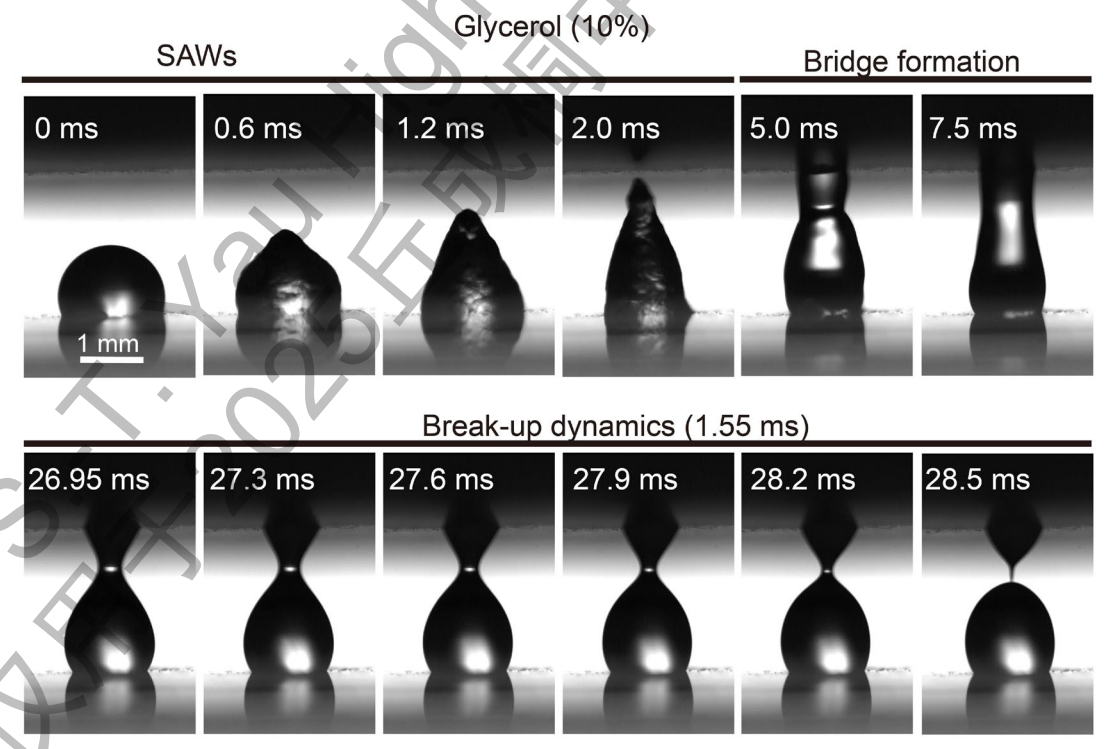


Figure 5.9. A montage of the behavior of a 2.0- μ L glycerol/water (10%) droplet subjected to a 2.0-ms SAW burst. It took 1.55 ms for the liquid filament to break up from an initial diameter of 430 μ m.

Similar to the above droplets, this 10% glycerol-water droplet continued to move upward after 2-ms SAW excitation. At \sim 2.5 ms, the vertex reached the opposing glass plate (Fig. 5.10). The average velocity during the pulse length was 0.3890 \pm 0.1907 m/s.

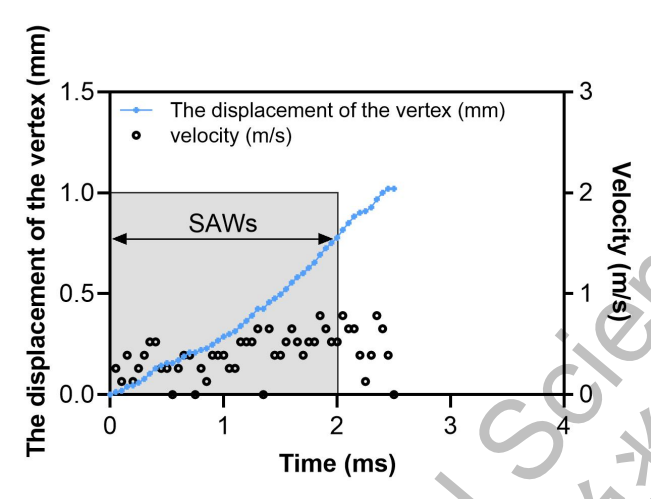


Figure 5.10. The displacement and velocity of the glycerol-water (10%) droplet vertex.

4) 16% Glycerol-water solution

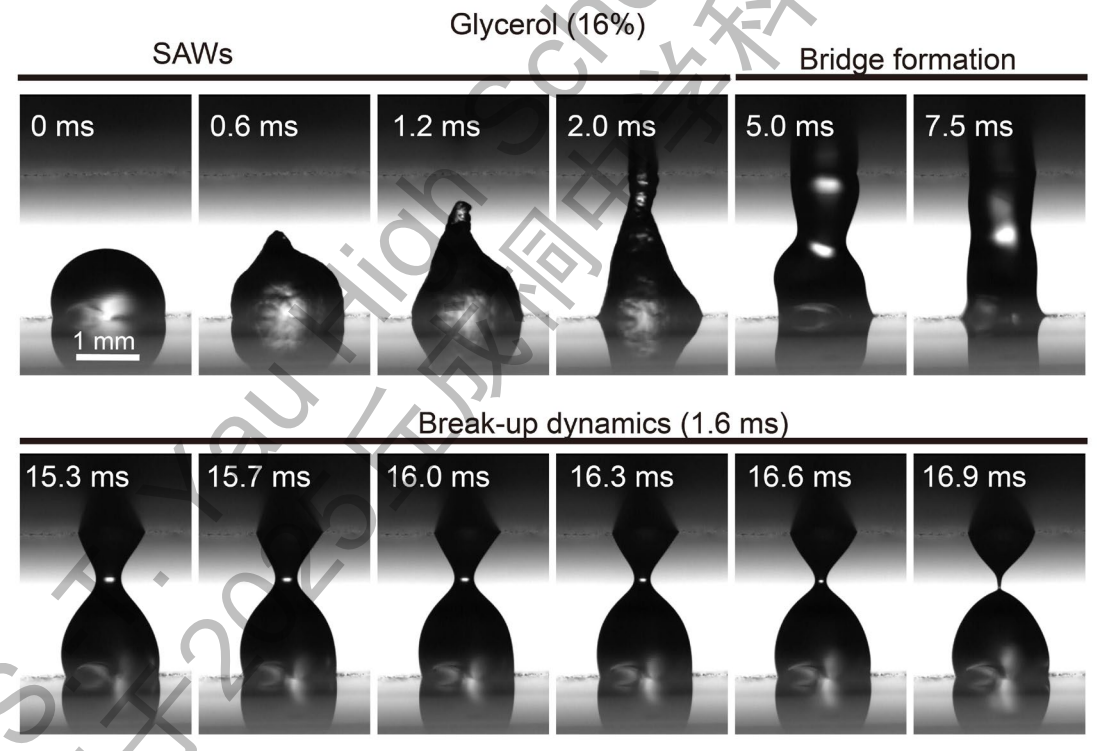


Figure 5.11. A montage of the behavior of a 2.0- μ L glycerol/water (16%) droplet subjected to a 2.0-ms SAW burst. It took 1.6 ms for the liquid filament to break up from an initial diameter of 430 μ m.

The glycerol concentration was further increased to 16%. At this concentration, the filament breakup time of the liquid bridge increased to 1.6 ms from the diameter being 430 μ m (Fig. 5.11). In contrast to the aforementioned droplet behavior, the 16% aqueous glycerol droplet moved upward at an increased speed

and made contact with the upper glass plate approximately 2 ms after motion initiation (Fig. 5.12). The average velocity during the pulse length was 0.6263 ± 0.2934 m/s.

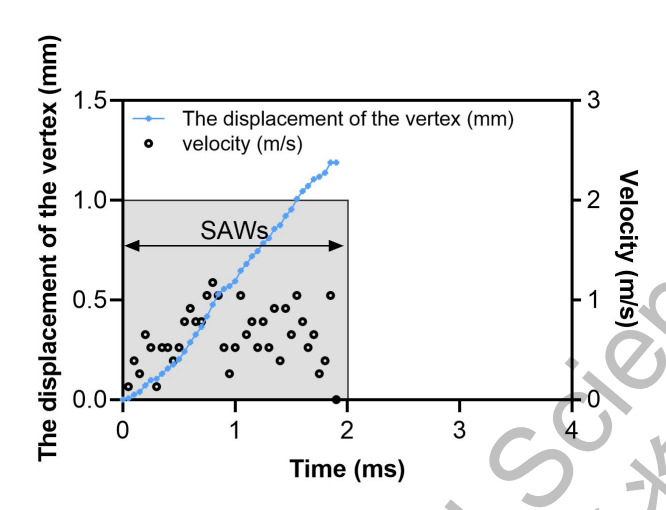


Figure 5.12. The displacement and velocity of the glycerol-water (16%) droplet vertex.

5) 18% Glycerol-water solution

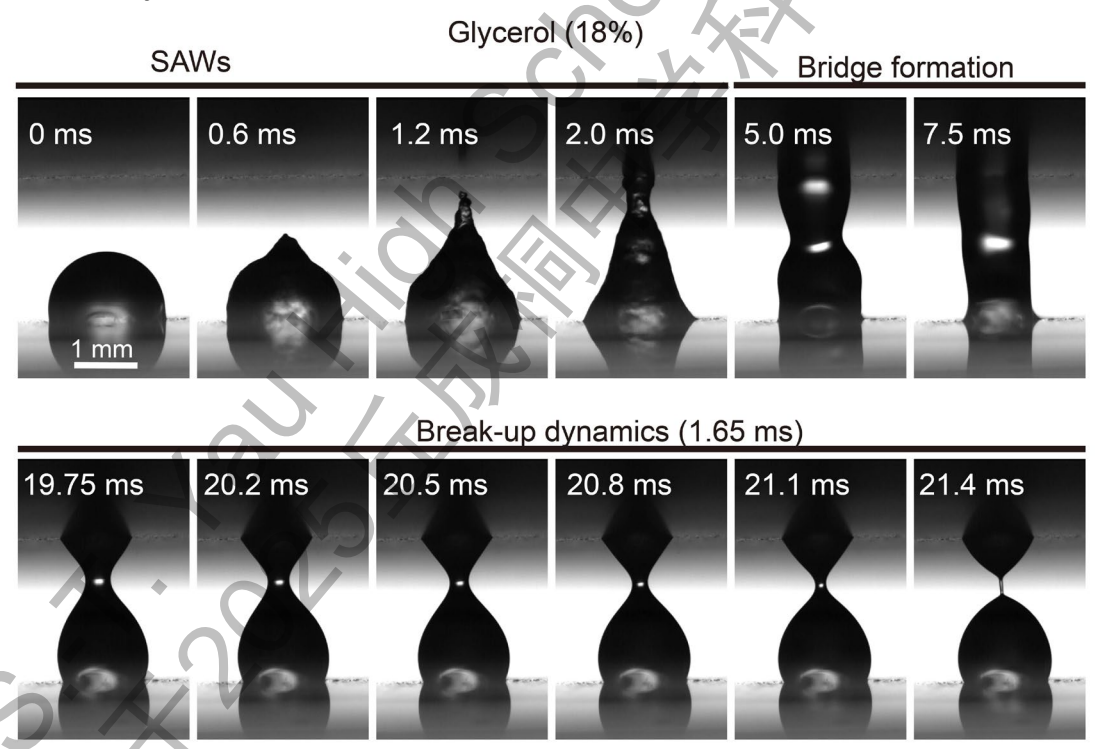


Figure 5.13. A montage of the behavior of a 2.0- μ L glycerol/water (18%) droplet subjected to a 2.0-ms SAW burst. It took 1.65 ms for the liquid filament to break up from an initial diameter of 430 μ m.

Next, the glycerol concentration was subsequently increased from 16% to 18%. At this concentration, the filament was observed to undergo breakup over a period of 1.65 ms, starting from a diameter of 430 μ m until its final rupture (Fig. 5.13). Similar to the behavior of the 16% aqueous glycerol droplet, the 18% aqueous

glycerol solution droplet contacted the upper glass plate in approximately 1.8 ms (Fig. 5.14). The average velocity during the pulse length was 0.7749 ± 0.4411 m/s.

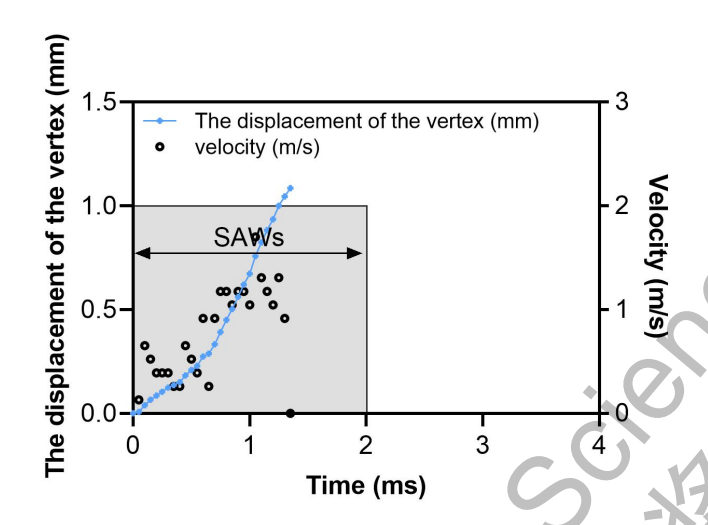


Figure 5.14. The displacement and velocity of the glycerol-water (18%) droplet vertex.

6) 20% Glycerol-water solution

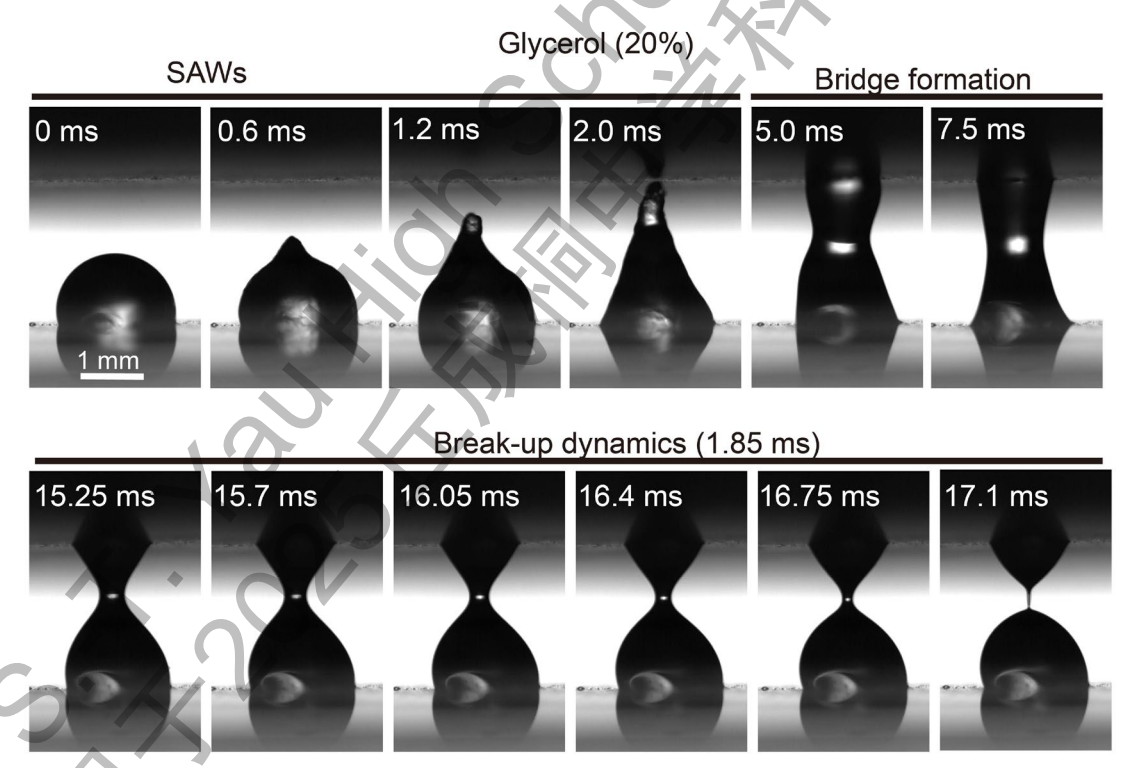


Figure 5.15 A montage of the behavior of a 2.0- μ L glycerol/water (20%) droplet subjected to a 2.0-ms SAW burst. It took 1.85 ms for the liquid filament to break up from an initial diameter of 430 μ m.

When the glycerol concentration was increased to 20% and 40%, the breakup times of the liquid filament increased significantly. From an initial diameter of 430 μ m until rupture, the process took 1.85 ms and 2.25 ms, respectively (Fig. 5.15 and

5.17). Similar to the behavior of the 18% aqueous glycerol droplet, the 20% and 40% aqueous glycerol solution droplets also contacted the upper glass plate in approximately 1.8 ms (Fig. 5.16 and 5.18). The average velocities during the pulse length were 0.6090 ± 0.3008 m/s and 0.7047 ± 0.4629 m/s, respectively.

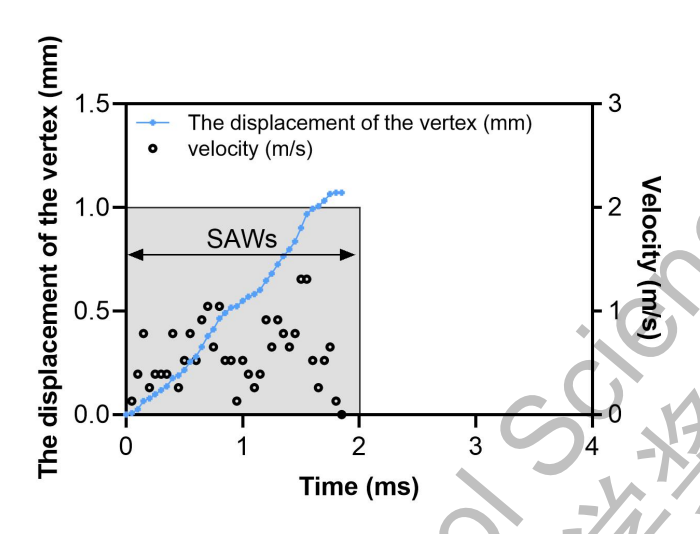


Figure 5.16. The displacement and velocity of the glycerol-water (20%) droplet vertex.

7) 40% Glycerol-water solution

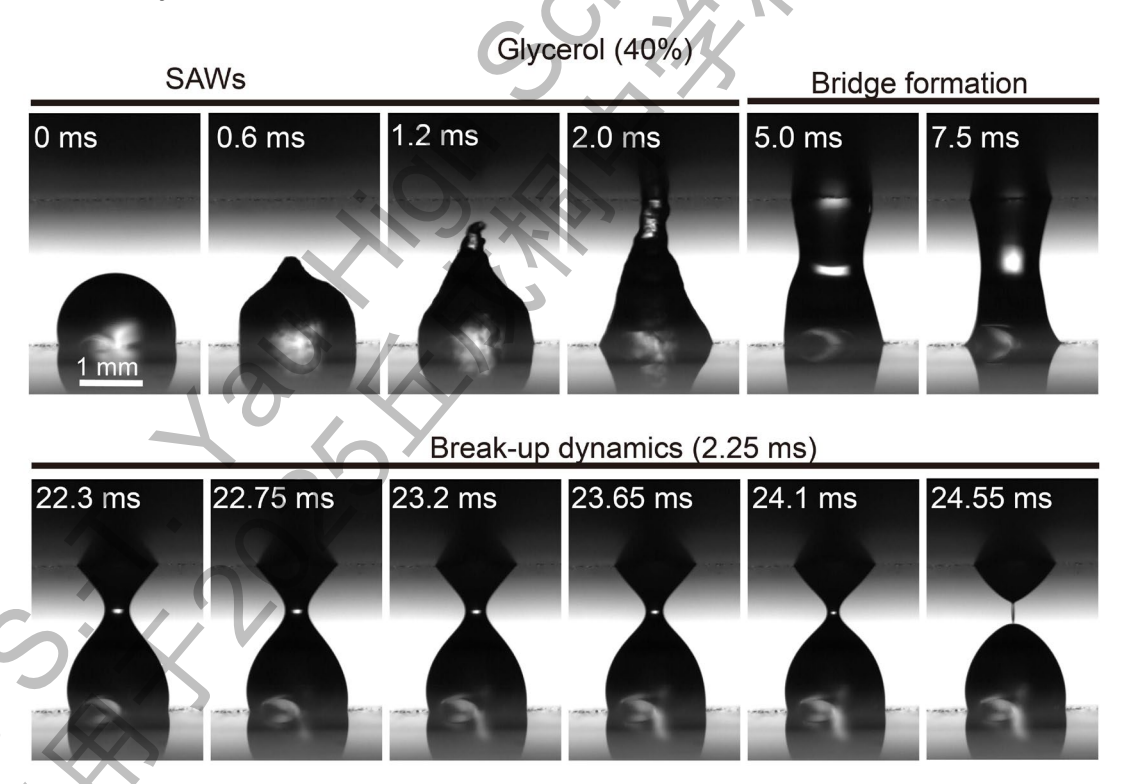


Figure 5.17. A montage of the behavior of a 2.0- μ L glycerol/water (40%) droplet subjected to a 2.0-ms SAW burst. It took 2.25 ms for the liquid filament to break up from an initial diameter of 430 μ m.

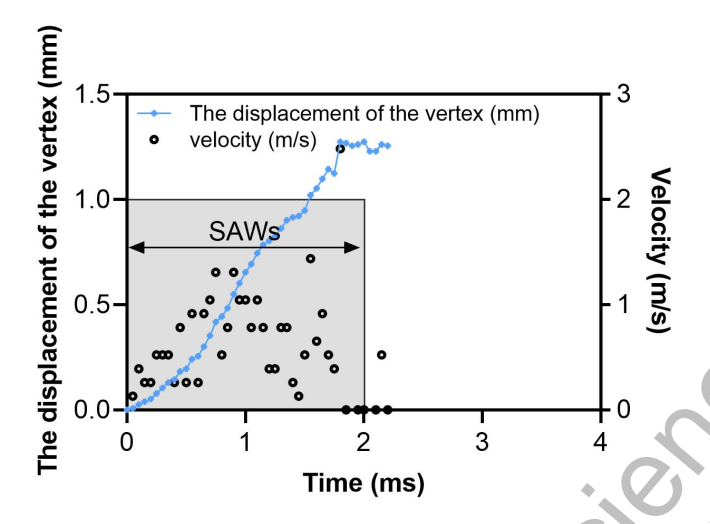


Figure 5.18. The displacement and velocity of the glycerol-water (40%) droplet vertex.

5.6 The curve of filament diameter versus time before breakup

Next, the dynamics of filament break-up were analyzed. From the images captured by the high-speed camera, a moment when the liquid bridge neck was still relatively thick was selected. The diameters at all subsequent time points were measured, resulting in the data presented in Fig. 5.19.

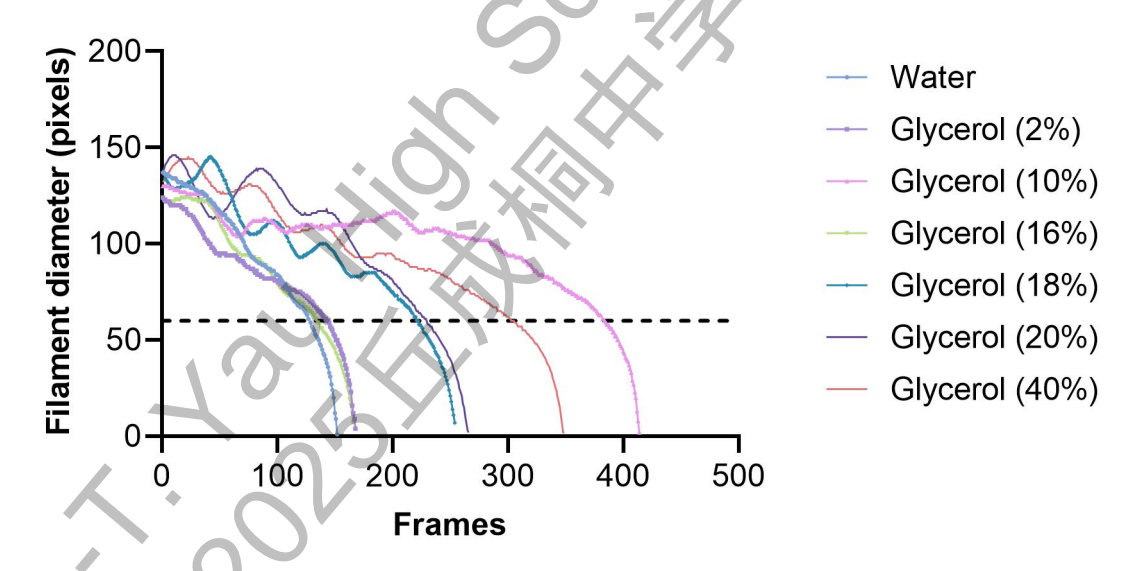


Figure 5.19. The variation curves of filament diameter over time.

Starting from a filament diameter of 120–150 pixels, the measured diameter exhibited an oscillatory decline over approximately 100–300 frames. This oscillation is attributed to the inertial effects resulting from the droplet motion actuated by the surface acoustic wave. Beyond a diameter of 60 pixels (430 μm), all the droplets no longer displayed oscillatory behaviors and instead demonstrated a stable thinning process. Therefore, this specific moment was selected as the starting point for the subsequent analysis of the breakup process.

The data from three repeated trials for each liquid were averaged to obtain the curve of filament diameter versus time prior to breakup, as shown in Fig. 5.20. As can be seen from this figure, the curve for the 2% glycerol-water mixture is clearly distinguishable from that of pure water. As the glycerol concentration increases further, the temporal curves of the samples become increasingly distinguishable. This provides an essential foundation for subsequent viscosity extraction.

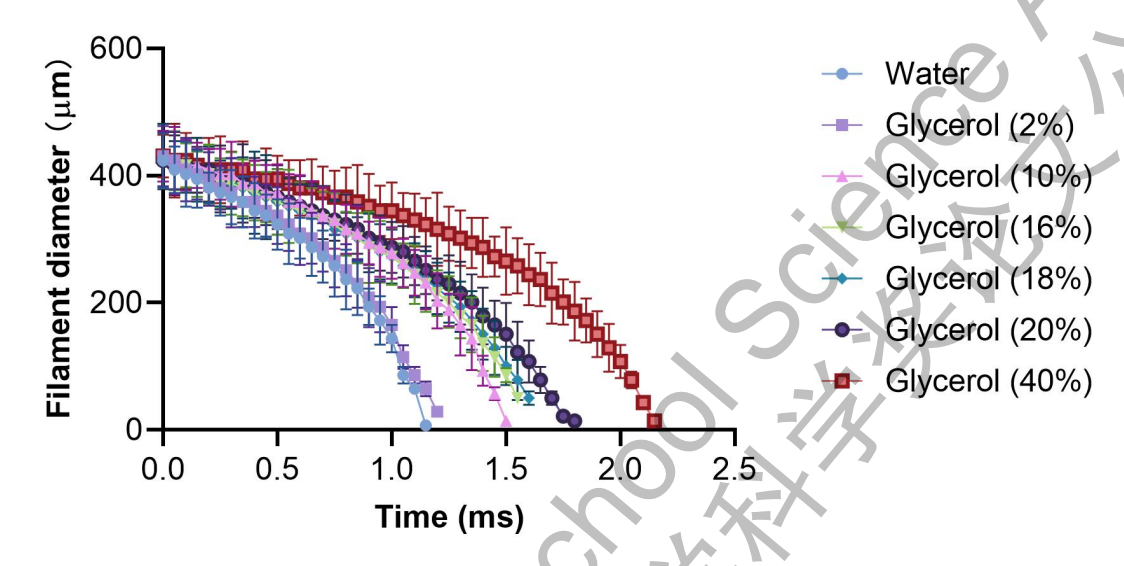


Figure 5.20. The curve of filament diameter versus time prior to breakup. The data from three repeated trials for each liquid were averaged.

5.7 The relationship of normalized half-time with the Oh number

According to the curve data in Fig. 5.20, the time point at which the filament diameter decreased to half of its initial diameter is defined as $t_{1/2}$. Then, a dimensionless half-time variable $t_{1/2}^*$ was normalized by the Rayleigh time τ_R . Table 3 summarizes the physical parameters of the seven liquid samples for subsequent analysis. Among these, the surface tension coefficient, density, and viscosity were obtained from the literature, respectively [15,16].

Table 3 Physica	l properties of th	e fluids used in t	his study
-----------------	--------------------	--------------------	-----------

	Fluid	+ σ	Density	Viscosity	τ_R (s)	$t_{1/2}^*$	R_0	Oh
	(volume	(N/m)	(kg/m^3)	(Pa·s)			(mm)	number
	fraction)							
	Water	0.07275	1000	0.001	0.003362	0.275107	0.9369	0.0038303
	(100%)							
	Glycerol	0.07281	1002.6	0.00095	0.003365	0.278578	0.9369	0.003623
	(2%)	<u></u>						
<	Glycerol	0.07313	1025.9	0.001219	0.003397	0.361377	0.937	0.004597
	(10%)							
	Glycerol	0.07348	1043.4	0.001496	0.003356	0.347319	0.962	0.005507
_	(16%)							

Glycerol	0.07359	1049.3	0.001607	0.003724	0.342382	0.991	0.005808
(18%)							
Glycerol	0.07368	1055.1	0.001729	0.003834	0.352133	1.009	0.006174
(20%)							
Glycerol	0.07154	1112	0.004046	0.003952	0.443852	1.002	0.014335
(40%)							

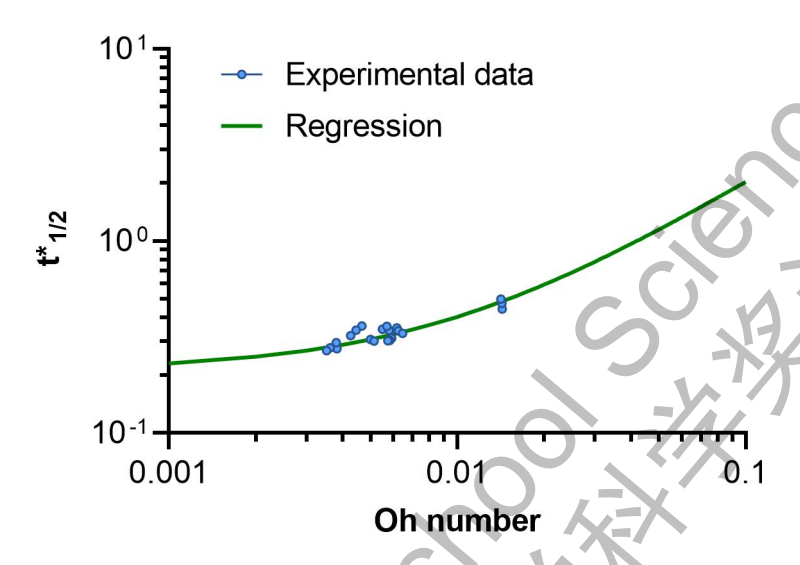


Figure 5.21 The relationship of the dimensionless half time $t_{1/2}^*$ for a filament to reach half its initial diameter and its Oh number for Newtonian standard solutions. The blue circle dots represent the experimental data. The green curve is the regression model of Equation 12.

Now, the relationship of the dimensionless half time $t_{1/2}^*$ and the Oh number could be established, as shown in Fig. 5.21. By regression analysis, the relationship could be expressed using the following equation:

$$t_{1/2}^* = \frac{0.211 + 19.450h + 7.0520h^2}{1 + 0h}. (12)$$

Therefore, based on this equation and Equation 14, the viscosity of the fluid could be calculated.

5.8 The viscosities extracted from artificial tear liquid

Due to the challenges associated with human tear collection, this study utilized polyvinyl alcohol (PVA) artificial tear fluid with a concentration of 1.4% PVA. After calibrating the relationship between the dimensionless half-time and the Oh number using Newtonian standard solutions, nine artificial tear samples were analyzed. Figure 5.22 depicts the jetting dynamics of Droplet No. 7, driven by SAW, and its subsequent filament breakup. The SAW pulse propelled the droplet until it contacted the upper glass plate, forming a stable liquid bridge at 7.5 ms. The bridge neck then rapidly thinned and ruptured within 2.20 ms. Figure 5.22b shows the filament diameter variation with time of the nine artificial tear samples. The half-time of these filaments to reach half their initial diameter ranges from 1.15 to 2.45

а Artificial tear No. 7 SAWs Bridge formation 0.6 ms 1.2 ms 2.0 ms 5.0 ms 7.5 ms 0 ms Break-up dynamics (2.20 ms) 11.75 ms 9.80 ms 10.90 ms 11.20 ms 11.50 ms 12.00 ms b 800 ET) 600 Filament diameter 600 400 400 200 200-

ms, with an average of 1.58 ms.

0.0 0.5 1.0 1.5

2.5 3.0

Time (ms)

Figure 5.22 (a) The montage of the behavior of artificial tear sample No. 7 (2.0 μ L) subjected to a 2.0-ms SAW burst. It took 2.20 ms for the liquid filament to break up from the initial time point. (b) Filament diameters of all nine samples (left) and the average one (right) versus time before breakup.

0.0 0.5 1.0 1.5 2.0

Time (ms)

2.5 3.0 3.5 4.0

The experimental procedure for determining viscosity involved three steps: First, the dimensionless half-time $t_{1/2}^*$ was computed from the parameters R_0 , $\tau_{1/2}$, τ_R . Second, this value was used in Equation 12 to solve for the Oh number. Finally, viscosity was calculated from the Oh number. The results are listed in Table

Table 4 Viscosities of artificial tear samples #

					P	
No.	R_0 (mm)	$\tau_{1/2} \; (ms)$	τ_R (ms)	$t_{1/2}^{*}$	Oh number	Viscosity
						Measured
Y						(mPa•s)
2	0.965	1.35	4.2	0.32	0.0058	1.31
3	0.952	2.45	4.11	0.6	0.0203	4.56

	4	0.956	1.95	4.14	0.47	0.0137	3.08
	5	0.984	1.3	4.32	0.3	0.0047	1.08
	6	0.988	1.15	4.35	0.26	0.0028	0.64
	7	0.963	1.61	4.19	0.38	0.0091	2.06
	8	0.978	1.275	4.28	0.3	0.0046	1.05
	9	0.946	1.81	4.07	0.44	0.0122	2.74
·	10	0.953	1.3	4.12	0.32	0.0054	1.22

^{#:} The video captured for Sample 1 was out of focus and therefore could not be used for analysis.

According to the box plot outlier criterion, the data point with a viscosity of 4.56 mPa·s was identified as an outlier. After its removal, the average viscosity of the artificial tears was calculated to be 1.65 ± 0.88 mPa·s.

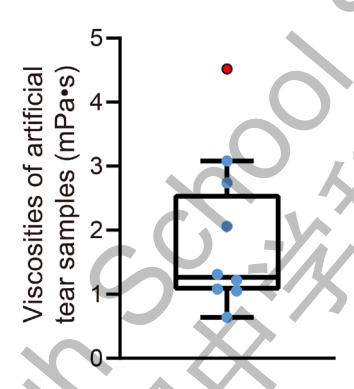


Figure 5.23 The box plot of the viscosities from the nine artificial tear samples. The red dot is an outlier data.

6. Discussion

Leveraging the energy of SAWs, this study achieved the controlled formation of a liquid bridge between two plates, thereby enabling viscosity measurements of low-viscosity fluids with volumes as small as microliters. To the best of our knowledge, this investigation introduces a novel technique with significant potential for future applications.

Measuring the viscosities of fluids with low viscosities has been challenging for an extended period. The CaBER rheology has only been developed in recent decades, which studies the evolution of surface tension-driven thinning of a liquid bridge under elongational deformation by separating two mechanical end plates [9]. It has been reported that CaBER was able to create observable bridges for fluid with viscosity as low as 11 mPa·s [17]. However, measuring the viscosity of even lower-viscosity aqueous solutions poses a significant challenge, a difficulty that is substantially compounded when working on liquid samples with microliter volumes. In fact, the formation of a liquid bridge at the microliter scale is the key

to solving this challenge. It is therefore encouraging to note that the methodology proposed in this study effectively accomplished this critical step by reliably generating liquid bridges using microliter-volume samples, thereby providing a robust solution for subsequent viscosity measurements.

Multiple factors, including but not limited to the fluid contact angle, the SAW amplitude, and the relative size of the droplet to the IDT aperture, collectively influence the amount of energy leaking into the droplet in a complex manner. To achieve the large contact angle necessary for droplet actuation, a hydrophobic coating on the LN substrate was essential; however, its thickness required precise control [5]. By carefully controlling the coating parameters (Teflon volume and spinning speed), sufficient contact angles were achieved to drive the droplet upward with an adequate aspect ratio. The amplitude of the SAWs is also a critical factor influencing the formation of the liquid bridge. At a fixed frequency, this amplitude is primarily determined by the pulse length and the magnitude of the excitation electrical signal's voltage. In this study, for a 2.0-µL water droplet resting on the substrate at a contact angle of 103°, whose diameter is ~1.8 mm, an aspect ratio larger than 1.67 could be achieved robustly when the pulse length was 2.0 ms at 18.41 MHz. However, a 1.5-ms pulse length did not generate elongation with such a high aspect ratio. When the pulse duration was extended to 5 ms, the droplet continued to move upward after contacting the upper endplate, which consequently hindered the stable formation of a liquid bridge. The sensitivity of liquid bridge formation to pulse duration was therefore a critical parameter that was optimized through extensive preliminary experimentation in this study. The input electric power is another crucial factor in the droplet elongation phenomenon. In Darmawan et al.'s study, which used 20-MHz focused IDTs with 80-degree arcs, similar to this study, only input power higher than 10 W could induce droplet jetting instead of droplet vibration phenomena [5]. In this study, 7 W of electrical power applied to the SAW device generated sufficient jetting of water droplets, comparable to the level observed in their research.

The term Weber number has been used to predict the jet phenomenon, defined as [6]:

$$We_j = \rho U_j^2 R_j / \sigma,$$

where U_j and R_j are the velocity and radius of the jet, respectively. Tan et al. utilized the Weber number to predict jet breakup modes [6]. They found that when the Weber number falls between 0.1 and 0.5, the jet pinches off at the leading edge, resulting in the ejection of a single droplet. In contrast, when the Weber number exceeds 1.0, the jet breaks up into multiple droplets due to Rayleigh-Plateau instability. As presented in Fig. 5.2, in the absence of the opposing glass plate, the average jet velocity ranged from approximately 0.3 to 0.7 m/s, corresponding to Weber numbers between 0.13 and 0.68. Under these conditions, the jet consistently exhibited single-droplet pinch-off. While the jet behavior consequently breaks up into multiple droplets, as shown in Fig. 5.1b, the maximum velocity within the initial 0.5 ms reached 1.83 m/s, with an average velocity of

 1.0070 ± 0.4777 m/s during this period (Fig. 6.1). The corresponding Weber number was 1.39, well above the threshold for jet breakup, leading to multidroplet formation. Therefore, this outcome aligns well with the predictions established by Tan et al.

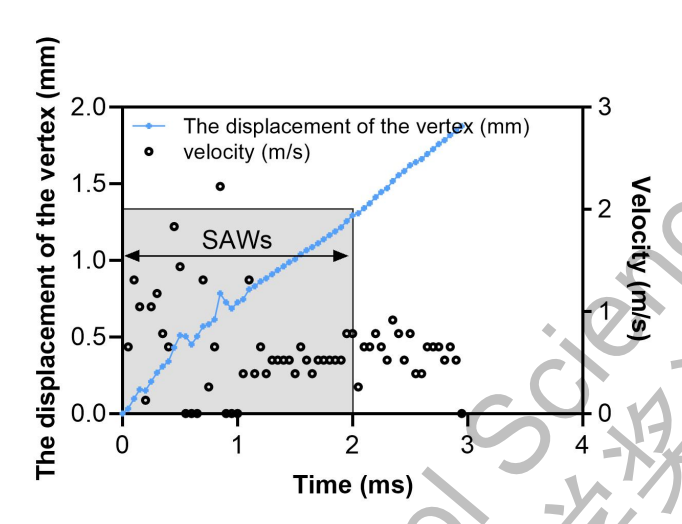


Figure 6.1 The displacement and velocity of the jet generated in Figure 5.1b.

The artificial tear solution used in this study contains 1.4% PVA. According to a white paper published by MilliporeSigma, the viscosities of 1.4% PVA eye drops range from 1.1 to 3.5 mPa·s, averaging at 2.21 ± 0.84 mPa·s [18]. In the present study, the measured viscosities of the nine samples ranged from 0.64 to 4.56 mPa·s. Aside from one outlier 4.56 mPa·s according the box plot criteria, the remaining values fell within the range of 0.6 to 3.1 mPa·s, averaging at 1.65 ± 0.88 mPa·s. Thus, the viscosities of the artificial tear samples with micro-liter scale volumes, as measured using the method established in this study, are in good agreement with the previously reported range. The 25.3% difference between the mean viscosity of the artificial tears measured in this study and that reported in the literature is likely attributable to differences in measurement methods. In addition, the study by Muñoz et al. reported a tear viscosity of 1.73 ± 0.61 mPa·s (range: 1.0-10.0) in healthy individuals [19], while A. J. Bron et al. reported a value of 1.87 ± 0.36 mPa·s (range: 1.2-2.4) [20]. Although this study measured artificial tears, the mean viscosity obtained is very close to that of healthy human tears. In contrast, the tear viscosity in patients with dry eye disease was measured by A. J. Bron et al. to be 1.03 ± 0.33 mPa·s, representing a 44.9% decrease [20]. Since surface acoustic waves can easily propel low-viscosity fluids to form a liquid bridge, the method proposed in this study is capable of measuring viscosities lower than that of water. This capability will be a focus of our subsequent work.

In this study, the 10 MHz and 30 MHz SAW devices exhibited significantly larger droplet actuation capability at 165 mV compared to the 20 MHz device. To find the underlying reason, I measured the impedance and phase angle of all six devices, as listed in Table 5. The results show that the 10 MHz device has a relatively high impedance with a phase angle reaching -80°, indicating pronounced

capacitive behavior [21]. This capacitive characteristic leads to increased power loss and reduced electromechanical conversion efficiency, thereby weakening the generation of acoustic streaming and reducing the actuation force on the droplet. Although the 30 MHz device exhibits near-ideal impedance, it still demonstrates capacitive behavior. Combined with its high operating frequency, this likely results in increased acoustic attenuation and more confined energy penetration into the droplet. Consequently, the acoustic streaming and resulting actuation force are significantly reduced, leading to less effective droplet driving compared to the 20 MHz device.

Table 5. Impedances of the six SAW devices

	10-1	10-2	20-1	20-2	30-1	30-2
z	92.7	139.5	85.3	53.4	48.9	45.9
θ	-80.6	-61.8	-71.2	-56.5	-62.6	-27.2

This study has several limitations. First, due to time constraints, impedance matching was not performed on the aforementioned devices, which is an aspect that requires improvement in future work. Second, as mentioned previously, the hydrophobic coating is critical; however, its thickness should not exceed one micrometer, as greater thickness could dampen surface acoustic wave propagation. Nonetheless, when the coating is made thinner, the vibration from the surface acoustic waves and the presence of droplets lead to coating degradation and detachment. As a result, the coating remains effective for only approximately 10 to 20 droplet actuation cycles, which considerably inconveniences experimentation. Furthermore, the initial position of the droplet is crucial. In this study, droplets were manually deposited via pipette, and contact with the hydrophobic surface often resulted in rolling, leading to inconsistent placement relative to the focal region of the IDTs. This is another key factor that warrants refinement in subsequent studies.

7. Conclusion

In this study, a novel approach was proposed and demonstrated for viscosity measurements of low-viscosity fluids with volumes as small as microliters. By employing SAWs, microliter-scale droplets were successfully actuated to form stable liquid bridges, which subsequently broke up within milliseconds. A high-speed camera captured this transient process, and the viscosity was determined by analyzing the temporal thinning behavior of the filament diameter. Using this method, glycerol-water solutions at various concentrations were tested to establish the relationship between the dimensionless half-time (required for a filament to reach half its initial diameter) and the Ohnesorge number. Finally, the technique was applied to characterize polyvinyl alcohol-based artificial tear samples, from which their average viscosity was derived. The findings confirm that the trajectories and thinning dynamics of liquid droplets, precisely controlled by high-frequency sound waves, serve as a highly sensitive proxy for quantifying fluid properties. Thus, this study truly embodies the idea of harnessing sound to

measure the unseen. The ability to extract rheology information from microscopic droplet behavior opens up new avenues for non-contact, high-throughput fluid analysis in lab-on-a-chip applications.

Acknowledgement

I gratefully acknowledge the support of my supervising teacher, Dr. Jian Hu, for his valuable suggestions on topic selection, data analysis, experimental problem-solving, and writing. I would also like to express my sincere gratitude to Prof. Chen Fu for providing me with the equipment to conduct the experiments without requiring anything in return. During this research project, whenever issues arose during experiments, the two supervisors consistently helped me identify the causes and continually refined the experimental methodology.

The research topic is based on my observations in daily life. During my participation in the migrant children community service, I noticed that one child's father often had red eyes. I learned that he works as a welder, a profession that frequently causes eye inflammation. Coincidentally, my grandfather also suffers from dry eye syndrome, though doctors have been unable to diagnose its specific subtype. Therefore, I reviewed the literature and found that these ocular conditions can lead to abnormal tear viscosity, measuring this parameter significant for diagnosis and treatment. This reminded me of a mischievous act from my childhood—playing with nasal mucus on my fingers. Following discussions with my mentor, I decided to use acoustic waves as an alternative to using a finger, enabling the formation of a liquid bridge with a minute amount of liquid for accurate viscosity measurement.

What I hadn't expected was the numerous challenges that arose in turning the idea into reality. Initially, I designed a one-sided SAW device, but it caused the droplet to move along the SAW propagation direction rather than elongate upward. Then, the design was improved by incorporating a pair of straight IDTs. However, this configuration still did not generate sufficient force to lift the droplet and form a liquid bridge of adequate aspect ratio. Finally, I designed an arc-shaped IDT that enabled the focusing of acoustic waves. This approach ultimately met the study's requirements. I still vividly remember the excitement I felt the moment the tiny droplet leaped upward. Then, the hydrophobic coating presented another unexpected challenge, which had been preventing the formation of the liquid bridge, and I had been searching for a long time. After experiencing the failure of damaging the SAW device through high-temperature drying, I eventually found a solution: using a relatively low temperature for an extended duration. In addition to these efforts, the parameter set presented in the report was ultimately identified through extensive experimental trials. As time passed, the research progressed more smoothly, and eventually, my vision became a reality. Seeing the final curve and the measured viscosity values, all the anxiety and doubt from earlier experimental failures turned into the most valuable tempering of my perseverance and skills.

I would also like to extend my thanks to my parents. Without their support, it would have been impossible to complete this research. I am genuinely grateful to the Yau committee for hosting this competition and providing all of us with such a valuable platform. This research experience has allowed me to deeply appreciate

the fascination of science and the importance of perseverance in overcoming challenges. I believe that this spirit of continuous inquiry and resilience will continue to guide me in all my future endeavors.

A. Author introduction

Zixuan Li

Grade: 12 Gender: Male

School: Shenzhen Middle School

Zixuan Li has a strong passion for physical acoustics and electromagnetism, which is reflected in his excellent academic record in physics at school and the achievement of earning top scores (5) on both AP Physics C: Mechanics and AP Physics C: Electricity & Magnetism.

Contribution: Zixuan Li proposed the idea of this study, conducted a literature review, performed all the experiments and simulations, collected the data, and wrote the research report.

B. Supervisor introduction

<u>Jian Hu</u>

Ph.D. in Physics from Tsinghua University, physics teacher at Shenzhen Middle School. He is primarily engaged in high school physics teaching and coaching physics competitions, with a research focus on astrophysics.

In this study, Dr. Hu played a crucial role in mentoring Zixuan Li throughout the project, providing invaluable guidance on selecting the research topic, analyzing data, conducting experiments, and writing the paper.

Chen Fu

Ph.D. in Engineering, Assistant Professor and Associate Researcher at the College of Physics and Optoelectronic Engineering, Shenzhen University. Recognized as a Shenzhen High-Level Overseas Talent, his primary research focuses on innovative piezoelectric thin films, acoustic MEMS devices, micro-vibration, and related signal excitation and detection.

In this study, Prof. Fu provided comprehensive guidance in theoretical foundations, data analysis, computational methods, and experimental design.

References

- [1] TFOS DEWS II Epidemiology Report, The Ocular Surface 15, 334 (2017).
- [2] L. E. Rodd, T. P. Scott, J. J. Cooper-White, and G. H. McKinley, Capillary Break-up Rheometry of Low-Viscosity Elastic Fluids, Applied Rheology **15**, 12 (2005).
- [3] J. Ning, Y. Lei, H. Hu, and C. Gai, A comprehensive review of surface acoustic waveenabled acoustic droplet ejection technology and its applications, Micromachines (Basel) 14, 1543 (2023).
- [4] A. Qi, L. Y. Yeo, and J. R. Friend, Interfacial destabilization and atomization driven by surface acoustic waves, Physics of Fluids **20**, 074103 (2008).
- [5] M. Darmawan and D. Byun, Focused surface acoustic wave induced jet formation on superhydrophobic surfaces, Microfluid Nanofluid 18, 1107 (2015).
- [6] M. K. Tan, J. R. Friend, and L. Y. Yeo, Interfacial jetting phenomena induced by focused surface vibrations, Phys. Rev. Lett. **103**, 024501 (2009).
- [7] B. von Boehn, M. Foerster, M. von Boehn, J. Prat, F. Macià, B. Casals, M. W. Khaliq, A. Hernández-Mínguez, L. Aballe, and R. Imbihl, On the promotion of catalytic reactions by surface acoustic waves, Angewandte Chemie International Edition **59**, 20224 (2020).
- [8] S. H. Sadek, H. H. Najafabadi, and F. J. Galindo-Rosales, Capillary breakup extensional electrorheometry (CaBEER), J. Rheol. **64**, 43 (2020).
- [9] S. L. Anna and G. H. McKinley, Elasto-capillary thinning and breakup of model elastic liquids, J. Rheol. **45**, 115 (2001).
- [10] J. Eggers, Nonlinear dynamics and breakup of free-surface flows, Rev. Mod. Phys. **69**, 865 (1997).
- [11] G. H. McKinley and A. Tripathi, How to extract the Newtonian viscosity from capillary breakup measurements in a filament rheometer, J. Rheol. **44**, 653 (2000).
- [12] A. G. McDonnell, T. C. Gopesh, J. Lo, M. O'Bryan, L. Y. Yeo, J. R. Friend, and R. Prabhakar, Motility induced changes in viscosity of suspensions of swimming microbes in extensional flows, Soft Matter **11**, 4658 (2015).
- [13] *SAW-Induced Streaming in a Droplet 2D Setup*, https://www.comsol.com/model/saw-induced-streaming-in-a-droplet-2d-setup-139131.
- [14] D. Lee, N. Lee, G. Choi, and H. H. Cho, Heat transfer characteristics of a focused surface acoustic wave (F-SAW) device for interfacial droplet jetting, Inventions 3, 38 (2018).
- [15] N.-S. Cheng, Formula for the Viscosity of a Glycerol–Water Mixture, Ind. Eng. Chem. Res. **47**, 3285 (2008).
- [16] A. Volk and C. J. Kähler, Density model for aqueous glycerol solutions, Exp Fluids **59**, 75 (2018).
- [17] C. Clasen, J. P. Plog, W.-M. Kulicke, M. Owens, C. Macosko, L. E. Scriven, M. Verani, and G. H. McKinley, How dilute are dilute solutions in extensional flows?, J. Rheol. 50, 849 (2006).
- [18] S. Rajput and H. Gosavi, Overcoming challenges in ophthalmic formulations through polymer selection a closer look at Polyvinyl Alcohol, (2022).
- [19] G. Muñoz, M. Millicovsky, J. Cerrudo, A. Peñalva, M. Machtey, J. Reta, R. Torres, D. Campana, and M. Zalazar, Exploring tear viscosity with quartz crystal microbalance technology, Rev. Sci. Instrum. **95**, 075107 (2024).

- [20] A. J. Bron and L. S. Mengher, The ocular surface in keratoconjunctivitis sicca, Eye **3**, 428 (1989).
- [21] T.-T. Wu, H.-T. Tang, Y.-Y. Chen, and P.-L. Liu, Analysis and design of focused interdigital transducers, IEEE Transactions on Ultrasonics, Ferroelectrics, and Frequency Control **52**, 1384 (2005).

Appendix

```
% Change input image path, output path, and image format
% Enter the file name of the starting frame
% Water Droplet Minimum Width Analysis (Displays Interactive Window and Result Curve
Simultaneously)
clear; clc; close all;
%% 1. Parameter Settings
imageFolder = 'D:\2025-07\21';
                                               % Image folder path
outputDir = 'D:\2025-07\result\21';
                                             % Result saving path
fileExt = '*.bmp';
                                              % Image format
                                                % Playback speed (seconds per frame)
displayDelay = 0.01;
saveResults = true;
                                                % Whether to save results
%% 2. Automatically Create Result Directory
if ~exist(outputDir, 'dir')
    mkdir(outputDir);
    fprintf('Result directory created: %s\n', outputDir)
else
    fprintf('Result directory already exists: %s\n', outputDir);
end
%% 3. Read and Sort Images
imageFiles = dir(fullfile(imageFolder, fileExt));
if isempty(imageFiles)
    error('Error: No %s format files found in %s', imageFolder, fileExt);
end
allFilenames = {imageFiles.name};
nums = cellfun(@(x) str2double(regexp(x, '\d+', 'match', 'once')), allFilenames);
validIdx = \sim isnan(nums);
imageFiles = imageFiles(validIdx);
allFilenames = allFilenames(validIdx);
nums = nums(validIdx);
%[~, sortIdx] = sort(nums); % Ascending order
[~, sortIdx] = sort(nums, 'descend'); % Descending order
imageFiles = imageFiles(sortIdx);
allFilenames = allFilenames(sortIdx);
totalFrames = length(imageFiles);
```

```
% Display file name range
minFileNum = min(nums);
maxFileNum = max(nums);
disp('=======');
disp(['Current image file name range: ', num2str(minFileNum), ' ~ ', num2str(maxFileNum)
disp('Example: xxxxx.bmp');
disp('=======');
%% 4. Input Starting Frame File Name
inputName = input('Please enter the full file name of the starting frame (e.g., xxxxxx.bmp):
% Automatically complete file extension
ext = fileExt(2:end);
if ~endsWith(inputName, ext)
    inputName = [inputName, ext];
end
% Check if file exists
startIdx = find(strcmp(allFilenames, inputName))
if isempty(startIdx)
    error('Error: File "%s" does not exist! Valid range: %d
        inputName, minFileNum, maxFileNum);
end
startIdx = startIdx(1);
%playFrames = startIdx:totalFrames;  % Playable frame range
playFrames = startIdx:-1:1; % From starting frame to 1st frame in descending order......
numPlayFrames = length(playFrames); % Total number of playable frames
% Display confirmation information
fprintf('\nStarting frame confirmed:\n');
fprintf(' File name: %s\n Sorted sequence number: Frame %d\n Number of playable
frames: %d\n', ...
    inputName, startIdx, numPlayFrames);
%% 5. Precompute Minimum Width for All Frames
fprintf('Preprocessing data for all frames...\n');
minWidths = NaN(1, numPlayFrames);
for i = 1:numPlayFrames
    frameIdx = playFrames(i);
    imgPath = fullfile(imageFolder, imageFiles(frameIdx).name);
    img = imread(imgPath);
    % Grayscale conversion
    if size(img, 3) == 3
```

```
imgGray = rgb2gray(img);
    else
         imgGray = img;
    end
    % Binarization and filling
    level = graythresh(imgGray);
    bwRaw = imbinarize(imgGray, level);
    bwDrop = \sim bwRaw;
    bwFilled = imfill(bwDrop, 'holes');
    % Calculate minimum width
    rowWidths = sum(bwFilled, 2);
    rowWidths = rowWidths(rowWidths > 0);
    if ~isempty(rowWidths)
         minWidths(i) = min(rowWidths);
    end
end
fprintf('Preprocessing completed!\n');
%% 6. Pre-draw Result Curve (Display Simultaneously with Interactive Window Without
Waiting)
relativeFrames = 1:numPlayFrames;
validIdx = ~isnan(minWidths);
if any(validIdx)
    % Plot width variation curve (figure 1)
    figure('Name', 'Water Droplet Minimum Width Variation', 'NumberTitle', 'off', ...
         'Position', [1200, 100, 800, 500]); % Display on the right without blocking the
interactive window
    plot(relativeFrames(validIdx), minWidths(validIdx), 'b-o', 'LineWidth', 1.5);
    xlabel('Frames After Starting Frame');
    ylabel('Minimum Width (pixels)');
    title('Water Droplet Minimum Width Variation Over Time');
    grid on;
    drawnow; % Display curve immediately
    warning('No valid data obtained, unable to plot result curve');
end
%% 8. Save Results (Execute After Interactive Window is Closed)
if saveResults && any(validIdx)
    csvPath = fullfile(outputDir, 'Water_Droplet_Minimum_Width_Results.csv');
    matPath = fullfile(outputDir, 'Water_Droplet_Minimum_Width_Results.mat');
    results = table(relativeFrames(validIdx)', minWidths(validIdx)', ...
```

```
'VariableNames', {'RelativeFrame', 'MinWidth_Pixel'});
    writetable(results, csvPath);
    save(matPath, 'results');
    fprintf('Results saved to:\n %s\n %s\n', csvPath, matPath);
end
%% Function Definitions (At the End of the File)
```

论文修改说明

评审专家意见如下:

改进建议: 1. 讨论温度对声波传播的影响(图 3.2 的仿真可补充温变参数); 2. 人工泪液样本量较小(图 5.22 仅 9 组数据); 3. 增加与传统粘度计的对比验证等; 4. 给出恰当的理论推导和解释,提升整体学术水平。

论文修改如下:

- 1. 回答:我加入了常见的三个气温温度 10,20 和 30℃ 下声表面波的传播数值仿真。随着气温的升高,焦点处的声表面波强度有所增强,表明漏进液滴内的能量有所减弱,但是整体来看,影响不大。此部分内容已在论文的第 8-9 页修改。
- 2. 回答:这是本研究的一个不足之处。由于实验条件限制,高速摄像机当时 是找了一个公司提供试用,期限比较短,所以只测了少量的样品。
- 3. 回答:通过查找文献, Millipore 公司发布过和本研究同样成分人工泪液的测量数据, 平均为 2.21 ± 0.84 mPa·s (范围为 1.1 到 3.5 mPa·s)[18]。本研究与其相差了 25.3%, 这可能是由于测量方法不同和测量条件不一致导致的,也对本研究后续进行更精准测量提出了要求。除此之外, Muñoz 等人的研究表明健康人的眼泪粘度经测量为 1.73 ± 0.61, 范围为 1.0-10.0 [19]; A. J. Bron 等人的测量结果显示健康人的眼泪粘度为 1.87 ± 0.36, 范围为 1.2-2.4 [20]。虽然本研究测量的是人工泪液,但是均值和健康人眼泪的粘度非常接近。而干眼症病人眼泪的粘度经 A. J. Bron 等人测量为 1.03 ± 0.33 mPa·s,下降了 44.9%。由于声表面波能够更容易推动低粘度流体向上形成液桥,因此本研究提出的方法能够测量比水粘度更低的流体粘度,这也是后续工作要继续进行的内容。此部分讨论增加在论文的第 34 页
- 4. 回答:理论推导和解释部分增加在论文的第6-7页。

